Techno-economics of solids-based thermochemical energy storage systems for large scale, high-temperature applications

N.B. When citing this work, cite the original published paper.

(article starts on next page)

Research papers

Techno-economics of solids-based thermochemical energy storage systems for large scale, high-temperature applications

Guillermo Martinez Castilla , Diana Carolina Guío-Pérez [*], Filip Johnsson , David Pallarès

Division of Energy Technology, Chalmers University of Technology, SE 41296 Gothenburg, Sweden

ABSTRACT

This work evaluates the techno-economic feasibility of the three most promising solids cycling systems (carbonates, thermally-reduced and chemically-reduced metal oxides) for thermochemical energy storage when deployed for large-scale applications with high-temperature operation. For each system, a specific material is selected (Ca, Co and Fe, respectively) and two process layouts are formulated: one focused on energy storage and one co-generating additional high-value byproducts (to offer CO_2 capture to nearby processes, production of pure O_2 and production of H_2 respectively). The study compares deployments sized to absorb 100 MW of solar power with an intermittency period of 12 h and dispatch it continuously as a constant high-temperature energy discharge. For each process layout, mass, energy and exergy balances are solved and the cost structure is calculated using a bottom-up approach.

The technical assessment shows the Co-based system to have the best performance (electrical efficiency up to 45 %) for sole energy storage due to its higher extent of reaction and energy density. The results show that the generation of valuable byproducts (to offer CO_2 capture and pure O_2, respectively) is done at the expense of electrical efficiency and dispatchability, although the Fe-based process with co-production of an energy carrier (H_2) reaches high energy efficiencies (>80 %). Nevertheless, the generation of valuable byproducts tends to improve the economic performance (reduction in breakeven electricity selling price - BESP) in all three systems. The results indicate that the deployment of chemically-charged (Fe-based) layouts involves up to 10 times larger costs than thermally-charged ones (Ca and Co) due to the cost of the reducing agent. Despite this, when involving production of H_2, the Fe-based process offers a significantly lower BESP than all other layouts. If high plant costs represent a financial barrier, Ca-based layout with CCS at the largest size investigated (250 MW) presents the lowest BESP among the rest of layouts investigated. Additionally, a parametric study reveals that the cost structure of the Ca-based process is the most robust to the variations considered in the study (costs of solid material, cooling water and heat input, as well as product selling prices).

1. Introduction

Renewable energy is an important component in the transition towards climate-neutral energy systems [1]. Wind and solar energy have increased their installed capacities significantly in the last decades and are foreseen to expand further: from a 25 % share in the global electricity mix in Year 2016 to an estimated 33 % in Year 2025 [2]. As this share increases, the electricity systems become increasingly characterized by the inherent variations of these electricity inputs resulting from fluctuating weather conditions which can vary in a scale of minute-to-minute to season-to-season [3]. These variations in the electricity input can cause instabilities in the grid [4] and therefore their

management is crucial for achieving a deep penetration of variable renewable electricity (VRE). Among different so called variation management strategies including flexibility both on supply and demand side [5], energy storage plays a key role by buffering the variations in generated power.

Within the field of energy storage, many electricity-to-electricity storage technologies have been developed in the past years, such as pumped hydropower [6], compressed air solutions [7] and electro-chemical batteries [8]. When it comes to storing an input in the form of solar energy, thermal energy storage solutions - both in the form of latent and sensible heat - are well-studied in concentrated solar power (CSP) plants [9]. However, the main drawback of thermal energy

storage technologies is the inherent energy losses, which hinder their full industrial deployment. In contrast, an energy storage technology that is gaining attraction in the last years is thermochemical energy storage (TCES), in which thermal and/or chemical energy is used (in the charging step) to drive an endothermic reaction. The chemical energy stored in the products resulting from this charging step is generally stable at ambient conditions and thus can be shipped or stored relatively easily. When energy is needed, the inverse (exothermic) reaction is promoted, releasing the stored energy (in the discharging step). TCES offers larger energy density (up to 10 times larger volumetric density and 50 larger gravimetric density [10,11]) than conventional thermal energy storage, as well as the possibility for long term storage [12]. Several projects have brought TCES technology to pilot scale [13] and demonstrated its potential for industrial scale implementation. Yet, storage including TCES is still not widely spread since it is generally too costly and electricity markets not volatile enough (as will be the case with further expansion of VRE) and there is therefore a need to further develop storage technologies to bring down costs and to include such which can provide storage which fits with wind power, requiring several days and up to a week of storage for which TCES is a potential candidate.

The most studied TCES processes to date are gas-solids systems (carbonates, metal oxides, hydroxides and metal hydrides) [14,15]. In this regard, fluidized bed (FB) units are shown to be a suitable technology for large-scale implementation of gas-solids systems in terms of both reactions and heat exchange, mainly due to their high mass and heat transfer capabilities [16]. Furthermore, the large mass flows in FB units due to the inherent presence of a large solids inventory provide a larger thermal inertia compared to other reactor technologies, and thus more uniform temperature fields which contribute to smoother operation. In addition, there is a long experience gained from the use of FB reactors in several industrial processes [17] (some of them directly related to gas-solids TCES, like Fe reduction [18]), which represents a potential for rapid deployment of new FB-based large-scale storage processes. At present, the use of FB reactors has been suggested for both steps (charging and discharging) of large-scale TCES systems [19], but burner-like gas-solids contactors are also being investigated (for the discharging step in metal oxide cycles [20]).

Regarding the applicability of the different gas-solids TCES systems, the turning temperature of the chemical system plays an important role as higher discharge temperatures enable a wider range of output vectors (i.e., district heating, steam, and electricity). In gas-solids TCES systems, hydroxides are only operable within 350–600 °C (besides offering poor powder properties [14]), while hydrides, despite operating at relatively high temperature levels, require H_2 storage (implying high costs) and present slow reaction kinetics [21]. Hence, according to several in-depth reviews [14,16,22], carbonates and metal oxides are the most promising gas-solids TCES systems when it comes to energy storage for high-temperature applications. These two systems have been intensively researched in the last decades for post-combustion carbon capture and chemical looping applications respectively (both based on FB reactors), which has led to extensive literature on operational experience. There is relatively abundant literature investigating the technical performance of the carbonate cycle typically referred to as calcium looping cycle (CaL) (see [13,23] and [24]), including pilot plant operation for CO_2 capture (1.7 MWth) [25] as well as for TCES (10 kWth). The latter has led to operational results in the fields of solar reactor design, plant operation and cost estimation [19]. Regarding the metal oxide cycle, many works have focused on testing the redox performance under different operational conditions. For example, Wong et al. [26] tested the potential of different metal oxides for TCES use, concluding that Co oxide showed the best technical results in terms of energy density and conversion. In this regard, Agrafiotis et al. [27,28] demonstrated the use of Co_3O_4 foams for TCES as a way to enhance the volumetric energy density and heat recovery properties, among others (against previous investigations utilizing Co-based pellets [29]). For both carbonate and metal oxide cycles, a substantial fraction of works has centered on the reactor design

instead, with special focus on the charging reactor as the transfer of non-dispatchable high-temperature heat into the reaction chamber remains a major challenge. For the case of solar irradiation input, the suggested designs can be divided between directly irradiated [30] and indirectly irradiated [31]. If the required heat is to be obtained from renewable electricity instead, in-situ oxy-combustion of green H_2 and directly electrified reactors (e.g. [32]) are the most investigated alternatives.

At the process level, a few works have carried out analysis of the technical feasibility of TCES applications (partially based of the more extensive literature found for the related fields of carbonate-based post-combustion carbon capture and of chemical looping [33]). Regarding carbonates, the works by Chacartegui et al. [34], Pascual et al. [35] and Rodrigues et al. [36] optimized the process performance under different operational modes, reporting higher thermodynamic efficiencies than conventional Rankine cycles. When it comes to metal oxides, Wu et al. [37] presented a thermodynamic assessment of a Co-based TCES system powered by wind or solar energy, which highlights the sensitivity of the process efficiency to the Co reactivity. Similarly, and focusing also on the Co_3O_4/CoO redox pair, Schrader et al. [38] reported a thermodynamic efficiency of 44 % when producing electricity from solar energy via a Brayton cycle. In a recent study, Martinez Castilla et al. [39] investigated the technical performance of implementing Fe-based TCES into district heating plants, finding out that the Fe inventories and flows required are much lower than those of biomass-fired plants. Bayon et al. [40] conducted a techno-economic study of carbonates and metal oxides for TCES from which they identified 8 systems with a storage cost under 25 \$/MJ excluding the cost of the reactors, i.e., only accounting for the material inventory and storage tanks. Related to the latter, the authors of the present work recently carried out a techno-economic analysis of a large-scale CaL process deployed for combined TCES and CCS reporting that the capital cost of the reactors was governing the investment cost structure [41].

Against this background, the authors identify that while many researchers have investigated the theoretical use of certain systems for TCES by investigating their energy densities and reaction kinetics, there is a big gap when it comes to connecting the chemical performance with the large-scale process feasibility. Hence, the aim of the present work is to assess the technical and economical performances of tentative large-scale process designs for the most promising gas-solids TCES systems for high-temperature applications. To do so, this paper evaluates systems of three types (carbonates, chemically-reduced metal oxides, and thermally-reduced metal oxides). For each type, different process layouts are formulated based on conclusions from previous works and assuming availability of a renewable, non-dispatchable, high-temperature heat input. Mass, energy, and exergy balances are then computed for each process layout, allowing a technical and economic comparison in terms of the energy and exergy efficiencies and the breakeven electricity selling price (BESP). Furthermore, the effect of key parameters on the calculated costs is evaluated through a parametric study. The outcome of this work is of special relevance as it provides data for assessing the competitiveness of large-scale gas-solids TCES technologies compared to other energy storage technologies.

2. Selection of solids systems

In the present work, previous literature is used to identify the most representative material for each of the three main types of high-temperature gas-solids TCES systems investigated in this work (carbonates, chemically-reduced metal oxides and thermally reduced metal oxides). The following sub-sections describe the motivation behind the solids material selection for each of the systems, based on the following general criteria:

- The material should have been previously suggested for large-scale deployment in terms of cost and availability.

- Sufficient literature concerning the testing of reactor and process conditions must be available.
- Only single-metal compounds are considered (i.e., mixtures and enhanced materials are disregarded).
- Both the charging and discharging reactions should have relatively fast kinetics and high conversion rates in order to minimize reactor dimensions.
- The temperature levels of the reactions should be within the range 650–1000 °C in order to i) match the temperatures reached at CSP solar receivers and ii) maximize the production of electricity at the discharging side.
- The solids should hold physical stability over large number of cycles.

2.1. Carbonates

Carbonates have been at the spotlight of high-temperature TCES research for years due to their high volumetric energy density, high conversion at low pressure, high operating temperatures, non-toxicity and non-corrosiveness [15]. Some of the most promising carbonates include those of Ca, Sr, Ba, Pb and Mg. Nevertheless, $CaCO_3$ is by far the most investigated for TCES due to the high availability and low price of natural Ca-based minerals such as limestone or dolomite [16]. Additionally, for Ca both directions of the reaction (calcination and carbonation, see Eq. (1)) present very high reversibility and fast kinetics [23]. Therefore, $CaO/CaCO_3$ is the selected carbonate system to be investigated in this work. Low cyclability, i.e., fast decay of the conversion degree with number of cycles, is noted as one main drawback [33].

$$CaCO_3 \leftrightarrow CaO + CO_2 \qquad \Delta H_R^0 = +178\,kJ/mol \qquad (1)$$
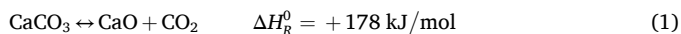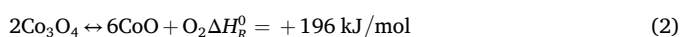
2.2. Metal oxides

Redox cycling of metal oxides sets a favorable basis for TCES systems due to their good performance at high temperatures (in terms of particle morphology and cyclability) and large gravimetric energy density. There is abundant literature regarding the use of these systems for applications such as chemical looping combustion [42], H_2 production via water splitting [43] and syngas production via carbon dioxide splitting [44]. Redox cycling of metal oxides is here separated into two types based on the mechanism used to drive the reduction step: thermal or chemical reduction.

2.2.1. Thermally-reduced metal oxides

Previous work [45] identified 16 single-metal oxides systems with thermally driven reduction at the temperatures relevant for the present work. Among those, the most widely investigated metal pairs are Co_3O_4/CoO, Mn_2O_3/Mn_3O_4, BaO_2/BaO and CuO/Cu_2O, due to their fast reaction kinetics, high energy densities and moderate overall costs [40]. When comparing these four systems in terms of energy density, Mn shows the lowest, while Co and Cu have exceptionally high values [11]. While the latter is relatively abundant, its transition temperature at atmospheric pressure ranges within 1030–1134 °C, which exceeds the limit of the present work (but might be of interest in advanced CSP plants). In terms of reversibility, Mn and Ba oxide systems show very poor performance as compared to Cu and Co. Schrader et al. [38] confirmed the technical feasibility of a Co oxide TCES plant at utility-scale by means of a thermodynamic analysis. In summary, Co_3O_4/CoO is often considered the most promising redox pair among thermally reduced metal oxides, despite its relatively low abundancy and its potentially carcinogenic properties [15], and is therefore selected for the present study. Eq. (2) shows the reversible redox reaction involved:

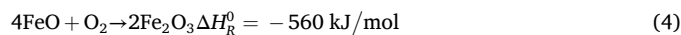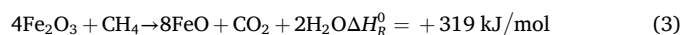$$2Co_3O_4 \leftrightarrow 6CoO + O_2 \Delta H_R^0 = +196\,kJ/mol \qquad (2)$$

2.2.2. Chemically-reduced metal oxides

For chemically reduced metal oxides, the input of high-temperature renewable heat is utilized to provide the heat of reaction for the endothermic reduction (charging) step of the redox cycle, but in addition to this a reducing agent is needed. Thus, the energy stored in the reduced material produced after the charging step stores the energy inputted by the high-temperature heat flow and the reducing agent together. For the energy stored in the reduced material, the share corresponding to the heat input has a maximum which is set by thermodynamics of each combination of solids and reducing agent.

There has been a vast number of publications testing different chemically reduced metal oxides with diverse fuels, reactor designs and process conditions (see review in [42]) during the last two decades due to their use in chemical looping processes. Chuayboon et al. [46] categorized the chemically reduced metals into two groups based on whether there is a phase change during the reduction process. For the so-called volatile oxides, (e.g., ZnO or MgO) the reduced species melt or vaporize and subsequently condense in the form of fine solids when temperature decreases, while non-volatile oxides (mostly ferrites and ceria materials) remain in the solid state. Considering the implications in terms of material losses and cyclability, non-volatile oxides are the preferred option for large-scale commercial deployment.

Chuayboon et al. [46] reviewed solar decarbonization processes and mapped routes combining solar energy with hydrocarbon feedstocks. Jafarian et al. proposed [47] and evaluated [48–50] a combined solar-CLC process for energy storage. In [50], they simulated different combinations of metal oxides and carbonaceous reducing agents, concluding that only CoO/Co, NiO/Ni and Fe_2O_3/Fe_3O_4 were potentially suitable to be reduced with natural gas to a sufficient extent. Jafarian et al. also found that the absorbed solar energy as compared to the chemical energy provided by the reducing agent (referred to as solar share) was generally low ($\sim$ 40%) and that it was maximized with the Fe system (solar shares up to 80 % were reported).

Based on the works cited above and the extensive literature on redox cycles of Fe oxides, FeO/Fe_2O_3 is here selected as the representative system for chemically reduced metal oxides (the intermediate level of oxidation, Fe_3O_4, is also considered, see Section 3.1). Note also that a reducing agent also needs to be selected. Gaseous agents are preferred as they exhibit faster kinetics and can act as fluidizing media in FB reactors [16]. CH_4 is selected for this work, since it is by far the most studied gaseous reducing agent in Fe oxide looping, and allows for a larger share of solar energy absorption [48]. This gas-solid choice is confirmed by previous studies that found Fe_3O_4 to offer the optimum conversion of CH_4 to combustion products as well as of steam to H_2 [51,52]. Eqs. (3) and (4) show the simplified reaction schemes for the reduction and oxidation processes, respectively.

$$4Fe_2O_3 + CH_4 \rightarrow 8FeO + CO_2 + 2H_2O \Delta H_R^0 = +319\,kJ/mol \qquad (3)$$

$$4FeO + O_2 \rightarrow 2Fe_2O_3 \Delta H_R^0 = -560\,kJ/mol \qquad (4)$$

3. Methods

The methods followed in the present work include: i) the formulation of six process layouts based on the three systems identified in Section 2, ii) the computation of the mass, energy and exergy balances, and iii) the computation of the economic performance indicators, all for each of the six layouts.

3.1. Formulation of the process layouts

The present work formulates six process layouts based upon literature that suggested process conditions and schemes for the three chemical systems identified in Section 2. In some cases, due to the boundary conditions of the current study, some operating conditions were modified, and assumptions made, e.g., when changing the reaction

media from one inert gas to another. In addition, for the sake of a fair technical and economic comparison between the processes, similar levels of heat integration and power cycles are applied to all processes.

Fig. 1 depicts the general TCES scheme applied to the processes in this work. For all the layouts studied, the charging section receives as input an intermittent high-temperature heat flow (see details on this in Section 3.2); this input could represent, for instance, a solar receiver in a CSP plant or a system of plasma torches in an electrified input scenario. Having set the reactor type to fluidized bed imposes the requirement for a fluidization gas flow in each of the reactors, regardless of this flow being reactive or inert. Storage of the solids material at ambient conditions is considered in all layouts, as this enables i) independent operation of the charging and discharging sections at all times, and ii) freighting of charged and discharged material without altering the energy and exergy efficiencies here computed (excluding the energy required for freighting). Efficient integration of solids storage at ambient conditions implies the presence of heat recovery between the hot and cold streams through the utilization of heat exchangers o different types: solids-solids (SS-HX), gas-solids (GS-HX), and gas-gas (GG-HX). Among the technical solutions for direct heat exchange between the two streams of solids, literature suggests a mixing seal valve configuration (not yet available at a commercial scale), or cyclonic preheaters (similar to those currently used in the cement industry) [13]. Solutions for indirect heat exchange appear closer to implementation and avoid undesired reactions. In this work, SS-HXs are assumed to operate as indirect contact heat exchangers with one intermediate heat transfer gas, i.e., as two direct-contacting gas-solids heat exchangers in series (for the gas phase). The impact of the net solids streams leaving and entering the process (i.e., the flow of makeup material) is outside the scope of this work, although its influence on the economic performance is estimated in a sensitivity analysis.

Some of the processes (hereafter called *TCES-focused*) are formulated to maximize the energy storage, while others offer the possibility to generate more valuable additional products or services (*by-product layouts*). Table 1 provides a list of the six process layouts studied in this

Table 1
Summary of the process layouts assessed in the present work.

Charging	Chemical system	Name	Additional product/ service
Thermal	$CaCO_3/CaO$	*CaL-TCES*[a]	–
		CaL-TCES-CCS[b]	CO_2 capture
	Co_3O_4/CoO	*CoL-TCES-OEA*[a]	Oxygen-enriched air
		CoL-TCES-O_2[b]	Oxygen
Chemical	$Fe_3O_4/FeO + CH_4$	*FeL-TCES*[a]	–
	$Fe_2O_3/Fe_3O_4/FeO + CH_4$	*FeL-TCES-H_2*[b]	Hydrogen

[a] *TCES-focused* layouts.
[b] *By-product* layouts.

work, with the corresponding naming, type of energy input required, chemical system, and additional product or service. Note that the *CoL-TCES-OEA* layout is here considered *TCES-focused* as it produces a simpler additional product as compared to the *CoL-TCES-O_2*. A detailed description of the layouts is provided in the subsections below.

3.1.1. Carbonates

3.1.1.1. CaL-TCES. The *CaL-TCES* layout formulated in this work is shown in Fig. 2 and based on the work by Chacartegui et al. [34]. The heat input is used to sustain the calciner (charging section) as well as to generate superheated steam to fluidize this reactor. Steam is selected as fluidization medium as it allows for a lower calcination temperature and increases the solids conversion in the carbonator [53]. The calciner conditions are set to 850 °C and 1 bar in order to yield full decomposition of the solids within a residence time below 10 min [23], with an outlet molar ratio of steam/$CaCO_3$ fixed to 1 following the recommendations by [53] in order to maximize the reactivity of the solid. The outlet gas stream is utilized to preheat a fraction (25 % according to [34]) of the total inflow of carbonated (discharged) solids ($CaCO_3$),
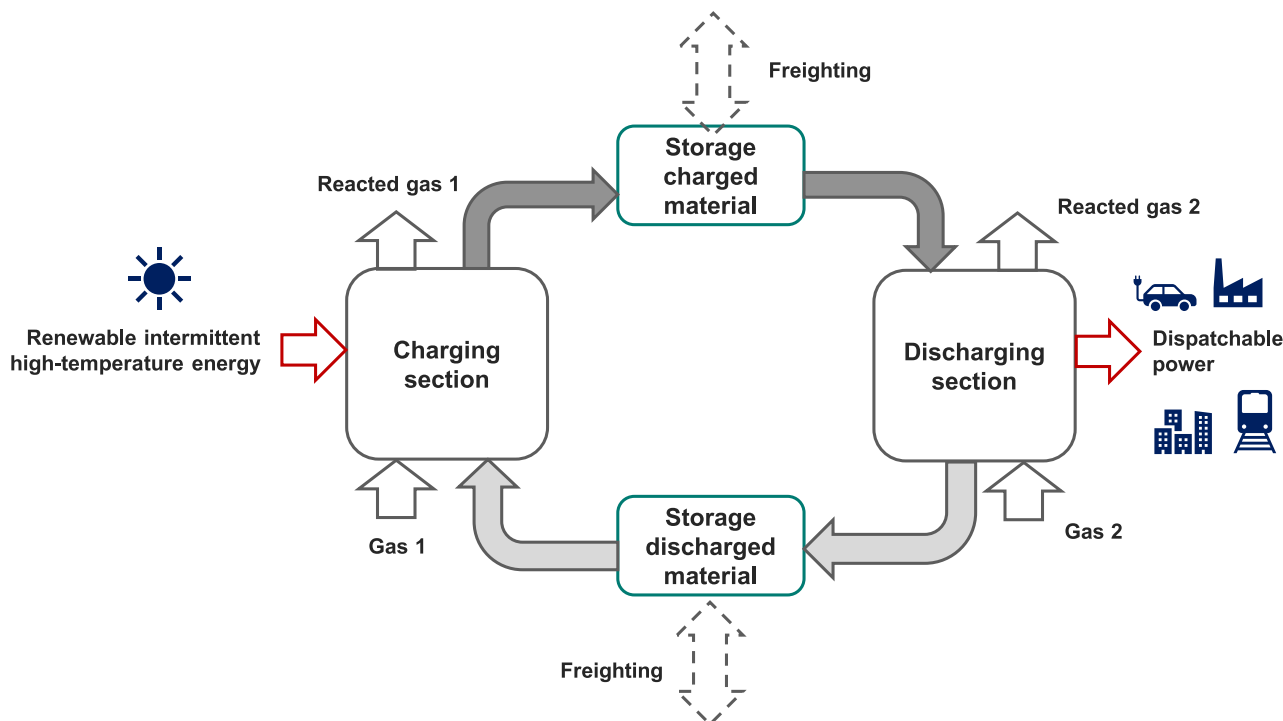

Fig. 1. General scheme of the TCES processes assessed in this work. The charging section is fed with renewable, intermittent high-temperature heat and the discharging section produces dispatchable electricity. Storage of charged and discharged solids at ambient conditions is considered since it allows for long-term storage, full decoupling of the charging and discharging sections, and solids freighting (outside the scope of this work).
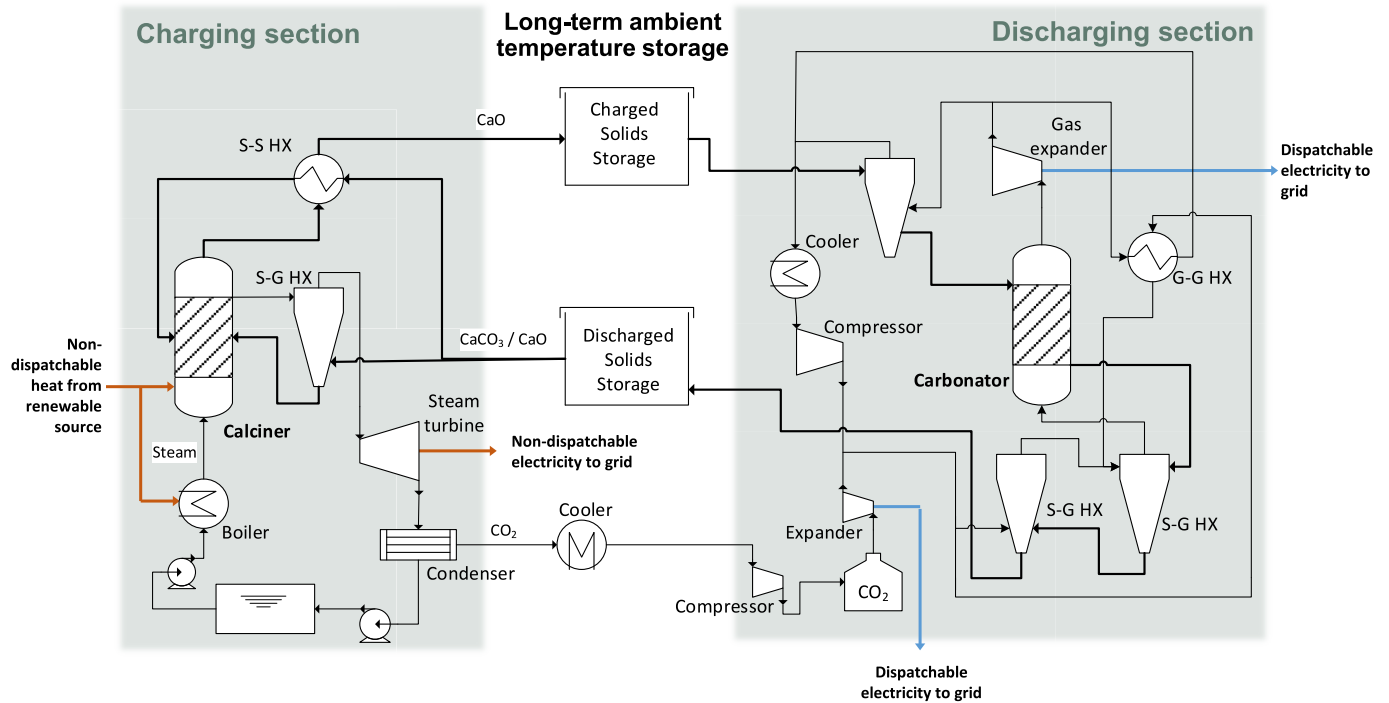
Fig. 2. Schematic of the *CaL-TCES* process layout. Calciner operates at T = 850 °C and P = 1 bar. Carbonator operates at T = 850 °C and P = 3.2 bar. S-G HX: solid-gas heat exchanger. S-S HX: solid-solid heat-exchanger. G-G HX: gas-gas heat exchanger. Bold lines represent solids streams.

before being expanded down to condensing pressure in a turbine. A water tank stores the condensate when the charging section is not operating. The rest of the incoming carbonated (discharged) solids (75 %) are preheated in a S-S HX by the solids stream outflowing the calciner. The CO_2 produced in the charging section is stored (cooled down and compressed up to 75 bar, according to the optimization results from [34]) for use in the decoupled carbonator (discharging section).

The carbonator operates at 850 °C and 3.2 bar and is fluidized with the stored CO_2 (after expansion, which recovers the net energy after subtracting the compression duty), yielding an average degree of conversion of 0.5 [34]. The inlet CO_2 is preheated in a series of S-G HXs and a G-G HX. Only a portion of the CO_2 injected to the carbonator reacts with the CaO to generate $CaCO_3$ (thus requiring a CO_2 recirculation

system) while the rest absorbs the heat generated by the carbonation reaction. The hot, pressurized outlet CO_2 is expanded down to 1 bar and used to preheat both the incoming calcined (charged) solids as well as the inlet CO_2.

3.1.1.2. CaL-TCES-CCS. The calcination/carbonation process can also be operated using flue gas from a nearby CO_2-emitting point. In this way, the energy storage scheme also serves the purpose of carbon capture. The process layout is depicted in Fig. 3 based on the process conditions suggested by Chacartegui et al. [34] and has been investigated in more detail by the authors in a former publication [41].

The charging section is the same as for the *CaL-TCES* scheme explained above, except that the CO_2 leaves the process for compression

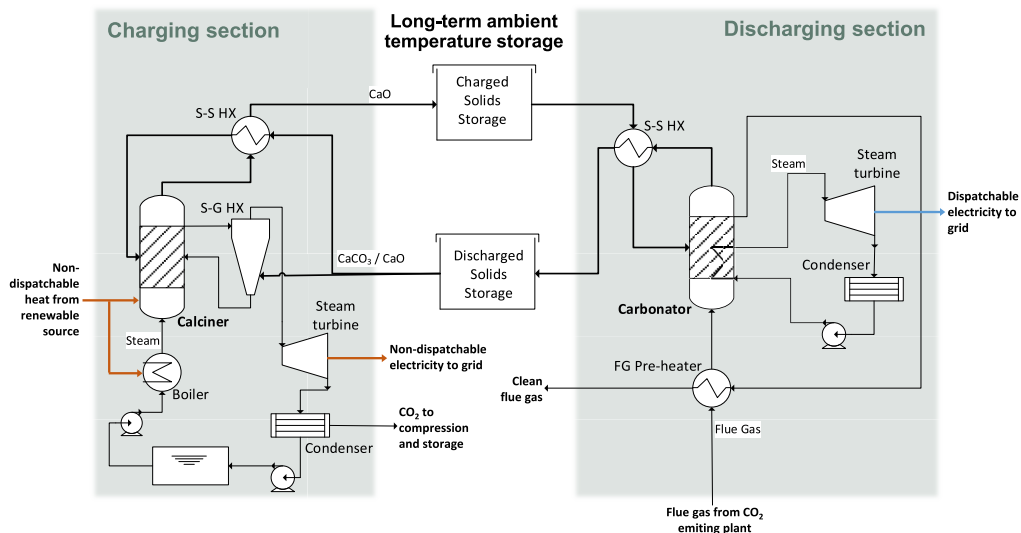**Fig. 3.** Schematic of the *CaL-TCES-CCS* process layout. Calciner operates at T = 850 °C and P = 1 bar. Carbonator operates at T = 650 °C and P = 1 bar. S-G HX: solid-gas heat exchanger. S-S HX: solid-solid heat-exchanger. FG: flue gas. Bold lines represent solids streams.

and storage (both steps lying outside the boundaries of this work). Regarding the discharging section, the main difference with respect to the *CaL-TCES* scheme is that the carbonator is fluidized with a CO_2-rich gas, e.g., combustion flue gas. Since the flue gas enters the plant at atmospheric conditions, the carbonator conditions are set to 650 °C and 1 bar. The CO_2 content of the inlet gas is assumed to be 15 %, for which a capture rate of 90 % can be assumed [54]. Likewise, a degree of conversion of 0.25 for the solids (from CaO to $CaCO_3$) can be assumed [13], i.e. much lower than that achieved in the *CaL-TCES* scheme but still higher than other CO_2-capture carbonation reactors as it is boosted by the steam calcination [13]. A Rankine cycle is selected for power generation, given the atmospheric pressure level of the gas. Note in Fig. 3 that a GG-HX has been placed to preheat the incoming flue gas so that the discharging section can operate with an inlet of cold flue gas.

3.1.2. Thermally-reduced metal oxides

3.1.2.1. CoL-TCES-OEA.
The *CoL-TCES-OEA* process layout shown in Fig. 4 is based on the reduction-oxidation of Co (II,III) oxide (see Eq. (2)). In the charging section, air is chosen as fluidization gas for the reduction reactor, thus oxygen-enriched air (OEA) is obtained as additional by-product with commercial value. The temperature and pressure conditions in the reduction reactor (980 °C and 1 bar) are chosen based on the thermodynamic studies setting 60 % O_2 content as target for the OEA produced [38,55]. These conditions yield 99 % conversion of the solids within 10 min, which is a feasible residence time for large-scale fluidized bed reactors. The charging section is completed by two heat exchangers (S-S and G-G HXs) pre-heating the inlet gas and solids streams with the outlet ones.

Regarding the discharging section, air is used to fluidize the oxidation reactor as well as to provide the O_2 required to oxidize the reduced solids (CoO) according to Eq. (2). Excess air (5 %) is introduced, as it is recommended to maximize solids conversion [37]. The outlet gas is used downstream in a Brayton cycle to produce the dispatchable power. The use of Brayton cycles in Co oxide loops has previously been suggested and investigated in [38]. Although Schrader et al. [38] suggested an oxidation pressure of 42 bar for maximizing energy efficiency, a pressure of 3 bar is selected in the present work as pressurizing the solids stream up to 42 bar might not be feasible in large-scale installations due to high operational costs. With this, a temperature of 850 °C is selected for the oxidation reactor, for which solids conversion of 90 % can be assumed in a timescale of about 10 min, according to thermodynamic

computations [55]. Analogous to the charging section, a S-S HX and a G-G HX are placed to recover a fraction of the sensible heat.

3.1.2.2. CoL-TCES-O2.
Based on the *CoL-TCES-OEA* scheme described above, the *CoL-TCES-O2* process (see Fig. 5) is a variant in which the charging section is modified to produce pure O_2 instead of OEA. For this, steam is chosen as the fluidization agent in the reduction reactor, as it can be condensed and separated from the O_2 stream. The reductor is still operated at atmospheric pressure, with the partial pressures of steam and O_2 set to 0.75 and 0.25 bar, respectively. Under such conditions, a temperature of 940 °C yields a solids conversion of 99 % (according to [55] and assuming that the thermodynamic computations remain valid when the O_2 desorption occurs in a steam atmosphere). The steam for fluidization is produced in a Rankine cycle that utilizes a fraction of the incoming available heat to evaporate the steam and superheat it up to 550 °C. A steam turbine is placed after the reactor to recover part of the energy and turned into non-dispatchable electricity. As depicted in Fig. 5, a water tank is added to store the liquid water when the charging section is not operating.

3.1.3. Chemically-reduced metal oxides

3.1.3.1. FeL-TCES.
The *FeL-TCES* process layout formulated in this work (see Fig. 6) is adapted from the one proposed by Liu et al. [51] and utilizes the thermodynamic data computed by Steinfeld et al. [56]. In the charging section of this scheme Fe (II,III) oxide, Fe_3O_4, is reduced to Fe (II) oxide, FeO, in a reactor fluidized with CH_4 which serves also as reducing agent. The reduction conditions are set to 1000 °C and 5 bar (which corresponds to the upper limits accepted in this work, see Section 2), which are the values suggested by Liu et al. [51] and under which they found that the maximum solids conversion was yielded through a CH_4-to-oxide ratio of 0.26, requiring a residence time about 15 min. The gas exiting the reactor consists of a mix of H_2O, CO, CO_2 and H_2, and is expanded down to atmospheric pressure (producing non-dispatchable electricity) and subsequently used to pre-heat the incoming CH_4. The present work does not include any further chemical valorization process of this stream.

For the discharging section, the oxidizer is operated at 900 °C and 1 bar (conditions typical of an air reactor in chemical looping combustion [42]), and heat is extracted via membrane tube walls that produce superheated steam that is fed into a turbine. Air preheated with the outlet gas provides the O_2 required for oxidating the solids stream, while

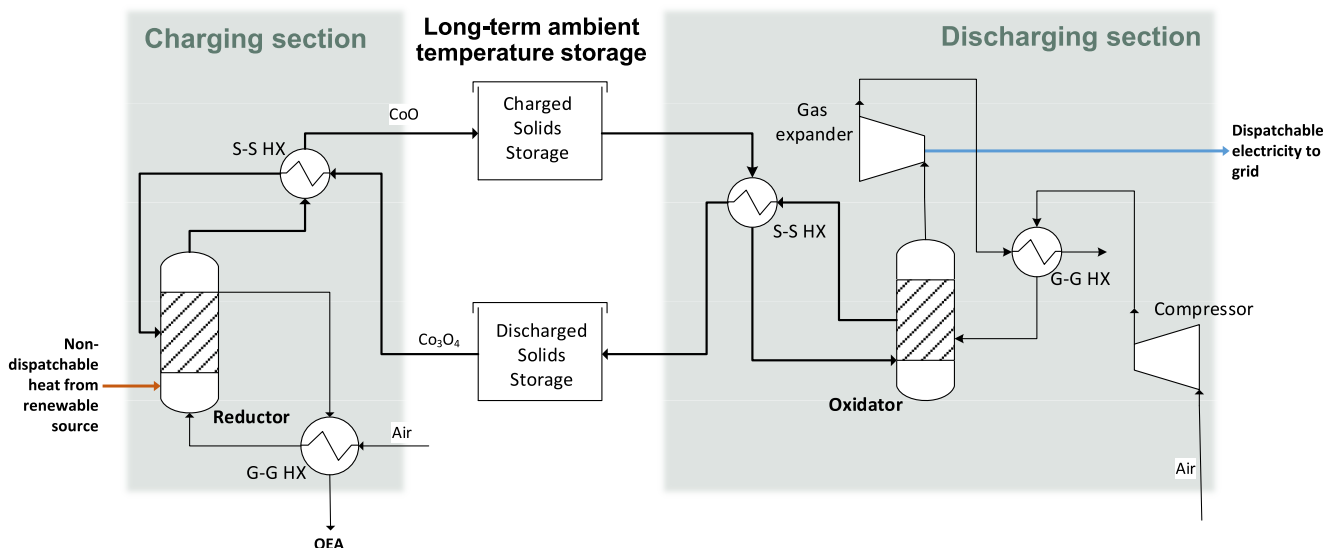**Fig. 4.** Schematic of the *CoL-TCES-OEA* process layout. Reductor operates at T = 980 °C and P = 1 bar. Oxidator operates at T = 850 °C and P = 3 bar. S-S HX: solid-solid heat-exchanger. G-G HX: gas-gas heat exchanger. Bold lines represent solids streams.

Fig. 5. Schematic of the *CoL-TCES-O₂* process layout. Reductor operates at T = 940 °C and P = 1 bar. Oxidator operates at T = 850 °C and P = 3 bar. S-S HX: solid-solid heat-exchanger. G-G HX: gas-gas heat exchanger. Bold lines represent solids streams.

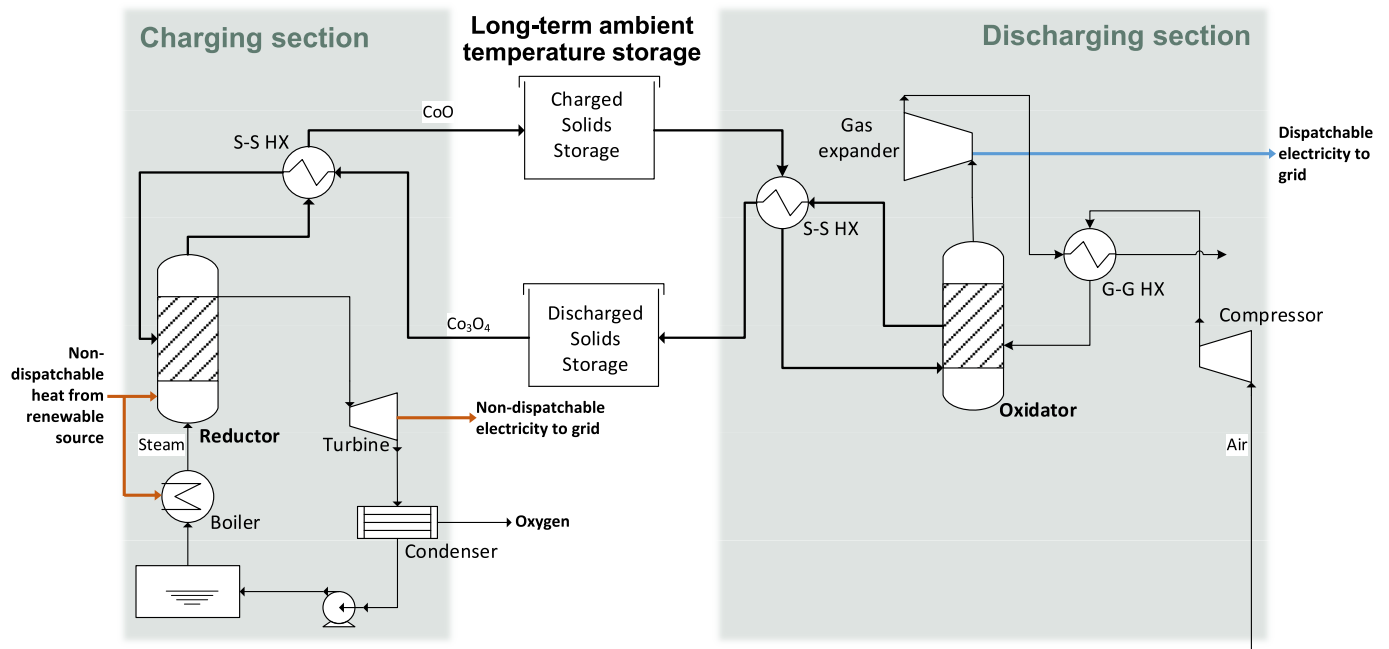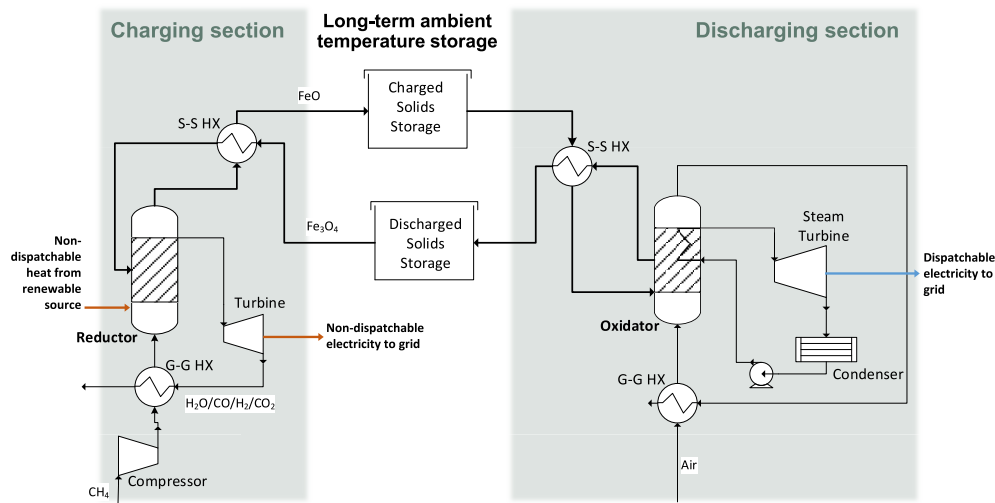**Fig. 6.** Schematic of the *FeL-TCES* process layout. Reductor operates at T = 1000 °C and P = 5 bar. Oxidator operates at T = 900 °C and P = 1 bar. S-S HX: solid-solid heat-exchanger. G-G HX: gas-gas heat exchanger. Bold lines represent solids streams.

serving as fluidization agent.

3.1.3.2. FeL-TCES-H₂. The *FeL-TCES-H₂* process (see Fig. 7) is based on the well-known concept of chemical looping water splitting with three reactors [33], thus exploiting the reaction scheme of the steam-iron process [57]. While those processes are meant for generating clean H₂ from a carbonaceous fuel, the *FeL-TCES-H₂* layout assessed here is meant to absorb high-temperature renewable energy (charging side) to output dispatchable electricity and H₂ on-demand (discharging side).

The charging section is kept the same as in the *FeL-TCES* scheme (Section 3.1.2.1). The discharging section consists of a two-step oxidation of the FeO. The first oxidation step occurs through water split in the steam reactor (SRx) which produces H₂ and is operated at 500 °C and 5 bar with a H₂O/FeO molar ratio of 1.8, following the recommendations from [51]. A turbine-compressor train is added to expand and condense

the steam that leaves the SRx, allowing the separation of H₂. The second step of the oxidation occurs through reacting the solids with O₂ in air. This takes place in the air reactor (ARx), which is operated as a conventional CLC air reactor (at 900 °C and 1 bar) and produces superheated steam for a Rankine cycle that produces dispatchable electricity. In the presented layout, the heat required for operation of the SRx is provided by superheating the inlet steam in the ARx. Lastly, the hot solids stream exiting the ARx is used to preheat the solids flows entering both the SRx and ARx, through two S-S HXs in series.

3.2. Mass, energy and exergy balances

The techno-economic analysis of the process layouts starts by the closure of mass, energy and exergy balances. The present section covers the methodology followed for the computation of such balances, for
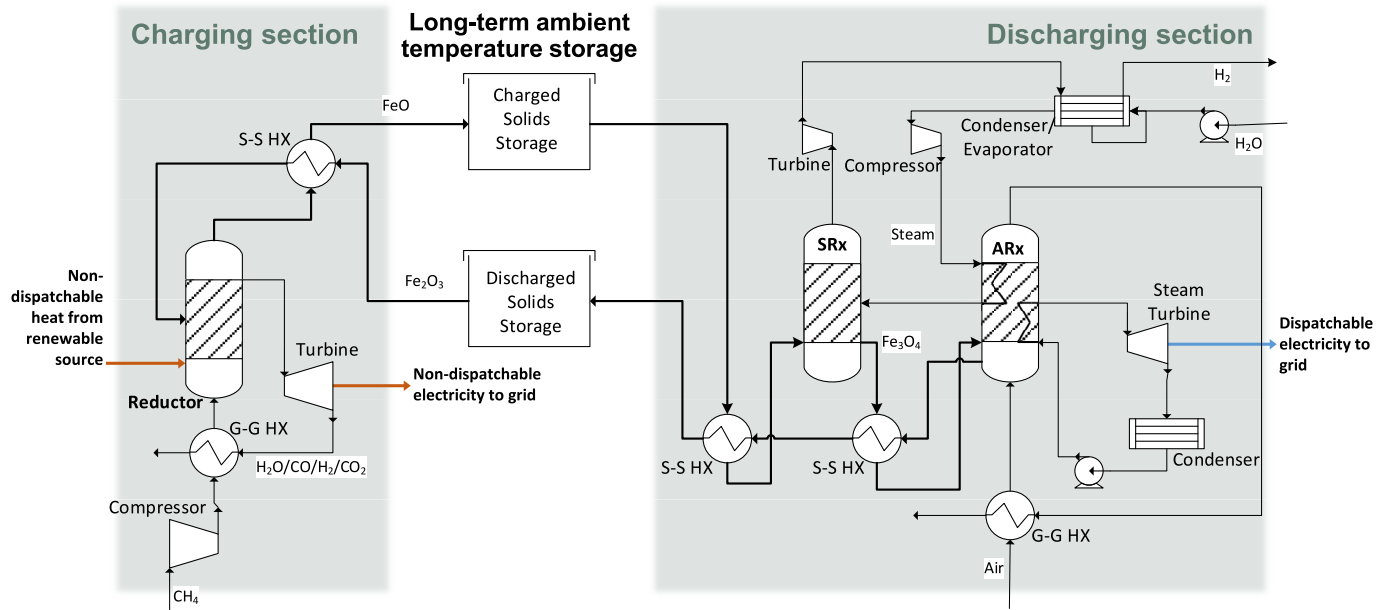
Fig. 7. Schematic of the *FeL-TCES-H₂* process layout. Reductor operates at T = 1000 °C and P = 5 bar. Steam reactor (SRx) operates at T = 500 °C and P = 5 bar. Air reactor (ARx) operates at T = 900 °C and P = 1 bar. S-S HX: solid-solid heat-exchanger. G-G HX: gas-gas heat exchanger. Bold lines represent solids streams.

which the main assumptions are listed below:

- 0-D components, i.e., uniform pressure and temperature
- No heat nor pressure drops in the reactors and pipelines
- No make-up/purge of solids material
- Static process operation (i.e., despite some units turning on and off, the dynamics of the process are not accounted, and each section is modelled as steady-state).

Table 2 lists the main process parameters and boundary conditions selected. For all processes, the energy input assumed consists of a heat flow, $Q_{in} = 100$ MW$_{th}$, intermittently available for continuous periods of

Table 2
Main parameters and assumptions considered for the mass, energy and exergy balance calculations. Values not referenced are either design choices or conventionally assumed within the field.

Parameter	Value	Reference
Net renewable heat input to the process, $\dot{Q}_{in}$(MW$_{th}$)	100 (50,250)[a]	–
Charging time, t_{ch} (h/day)	12	–
Discharging time, t_{disch} (h/day)	24	–
Storage temperature (°C)	20	–
Minimum temperature difference S-S HX (°C)	20	–
Minimum temperature difference S-G HX (°C)	20	–
Minimum temperature difference G-G HX and condensers (°C)	15	–
S-G heat transfer coefficient (W/(m²K))	480	[17]
Fluid-fluid heat transfer coefficient (W/(m²K))	1500	[58]
Rankine cycle live steam temperature (°C)	550	–
Rankine cycle live steam pressure (bar)	120	–
Solids porosity (solids volume/total volume)	0.5	[40]
Turbomachinery isentropic efficiency (%)	89	[59]
Electric generator efficiency (%)	98.5	–
Solids conveying energy requirement (MJ/t/100 m)	10	[34]
Equivalent solids conveying length (m)	100	[34]
Cooling water temperature (°C)	20	–
Cooling water discharge temperature (°C)	70	–
Cooling water pumping distance (m)	1000	–

[a] Three different values for $\dot{Q}_{in}$ are considered in order to assess the impact of the net energy input.

$t_{ch} = 12$ h/day, at a temperature level sufficient for the charging of the solids (T_{ch}, which depends on the chemical system selected). The discharging section is for all processes assumed to operate steadily for $t_{disch} = 24$ h/day. These assumptions represent a simplification of real scenarios in which both the input energy flow and the demand-side curve vary continuously over time. Assessing any such real scenario requires the use of a dynamic model, which lies outside the scope of the present work. Nevertheless, the assumption described above is found adequate for the aim of this work, since the corresponding analysis evaluates an average performance and thus provides representative values necessary for a first assessment of the processes. The impact of the heat input on the economic feasibility of the processes is evaluated by considering Q_{in}-values of 50 and 250 MW too in the analysis.

In all processes considered, all the solids leaving a (charging/discharging) section are assumed to be cooled down to ambient conditions. In practice, a fraction of solids could be directly fed hot into the other section, which would improve the energy and exergy efficiencies. The optimization on which share of the solids is stored or directly sent to reaction needs to account for the dynamics of the heat input and power demand, which lies outside the scope of the current work.

The extent of conversion in each of the reactors is a critical parameter as it impacts to a large extent the closure of the mass and energy balances (see Supplementary material). Since the reactions taking place are fundamentally driven by equilibrium, the composition at the outlet of the reactor is consequence of the pressure and temperature conditions and a given residence time and does not depend on the composition of

Table 3
Summary of the method utilized to model the extent of reaction in each of the process assessed.

Process scheme	Method	References
CaL-TCES	Known extent of reactions	[34]
CaL-TCES-CCS		[13]
CoL-TCES-OEA		[55]
CoL-TCES-O₂		[55]
FeL-TCES	Equilibrium conditions (minimization of Gibbs free energy)	[51]
FeL-TCES-H₂		[51]

the inlet stream. In this work the extent of conversion of each system (see Table 3) is retrieved from literature whenever available, or calculated through minimization of Gibbs-free energy, i.e., assumed to yield equilibrium conditions.

Given the assumptions and parameters presented above, mass and energy balances are computed for each of the reactors (see Supplementary material for details). In the charging reactor, the molar flow rate of solids is computed from the known heat input and extent of reaction. In the discharging reactor, the molar flow of solids is double of that computed for the charging section, according to the mass balance expressed by Eq. (5) and the charging and discharging time set (see Table 2).

$$F_{disch} \cdot t_{disch} = F_{ch} \cdot t_{ch} \tag{5}$$

Based on the mass and energy balances described above, two performance metrics are computed to assess the energy performance of each process layout. First, the overall energy efficiency, η_{tot}, is computed according to Eq. (6), which includes the time-weighted average of the energy inputs and outputs,

$$\eta_t = \frac{\dot{W}_{net,ch} t_{ch} + \left(\dot{W}_{net,disch} + \dot{Q}_{chem,out} \right) t_{disch}}{\left(\dot{Q}_{in} + \dot{Q}_{chem,in} \right) t_{ch}} \tag{6}$$

where $\dot{W}_{net}$ represents the net electrical output of each section (i.e., subtracting parasitic electricity consumption) and $\dot{Q}_{in}$ represents the heat input. Chemically-charged process layouts also include chemical energy input and output, $\dot{Q}_{chem,in}$ and $\dot{Q}_{chem,out}$. Note that the output heat streams are not considered as valuable output in this work as a location with high solar share and low heat demand is assumed.

Second, the dispatchability ratio r_{disp} evaluates how the energy input is distributed between dispatchable and non-dispatchable electricity and is defined according to Eq. (7), where $\dot{W}_{net,disch}$ and $\dot{W}_{net,ch}$ represent the electricity produced in the discharging and charging sections, respectively. This factor also represents the fraction of absorbed energy that can be delivered with a displacement in time (and potentially space if the stored solids material is freighted), i.e., a metric of how much non-dispatchable energy input is actually stored [39].

$$r_{disp} = \frac{\dot{W}_{net,disch} t_{disch}}{\dot{W}_{net,ch} t_{ch} + \dot{W}_{net,disch} t_{disch}} \tag{7}$$

In this work, an exergy analysis is carried out to analyze the distribution of useful energy and the generated irreversibility throughout the chain of energy transformations. The exergy of every stream is calculated according to Eq. (8) accounting for the physical exergy $\dot{E}_{phys}$, and the chemical exergy $\dot{E}_{chem}$. The contribution of the kinetic and potential exergy is here disregarded as the changes in elevation and velocity are neglected. When referring to a mixture of fluids, the physical and chemical exergies are calculated as shown in Eqs. (9) and (10) [60], where the subindex i represents each component of the mixture, 0 represents the dead state (in this work selected for a pressure and temperature of 1 bar and 20 °C, respectively) and $E_{0,i}$ is the standard chemical exergy of the i-th species, here taken from Szargut [61].

$$\dot{E}_{tot} = \dot{E}_{chem} + \dot{E}_{phys} \tag{8}$$

$$\dot{E}_{phys} = \sum_i x_i \left[(h_i - h_{0,i}) - T_0 (s_i - s_{0,i}) \right] \tag{9}$$

$$\dot{E}_{chem} = \sum_i x_i \left[E_{0,i} + \varphi RT_0 ln \frac{p_0}{p_{00}} \right] \tag{10}$$

This work applies the exergy balance at a process level as defined in Eq. (11), where $\dot{E}_{in,i}$ and $\dot{E}_{out,i}$ refer to the exergy of the inlet and outlet material streams of the process, $\dot{W}$ represents the work (electricity)

produced by the process, $\dot{Q}$ represents the work obtainable from the heat fluxes to/from the process and $I_{destroyed}$ is the irreversibility generated within the process.

$$\sum_i \left(\dot{E}_{out,i} - \dot{E}_{in,i} \right) = \sum_i \left(1 - \frac{T_0}{T_i} \right) \dot{Q}_i + \sum_i \dot{W}_i + I_{destroyed} \tag{11}$$

Two additional metrics to evaluate process performance based on the exergy balance are added: the total exergy efficiency, $\eta_{ex,t}$ (Eq. (12), which includes all outlet streams), and the functional exergy efficiency, $\eta_{ex,f}$ (Eq. (13), which accounts only for outlet streams considered as valuable products).

$$\eta_{ex,t} = \frac{\sum\limits_i \dot{E}_{out,i}}{\sum\limits_i \dot{E}_{in,i}} \tag{12}$$

$$\eta_{ex,f} = \frac{\sum\limits_i \dot{E}_{product,i}}{\sum\limits_i \dot{E}_{in,i}} \tag{13}$$

Fig. 8 schematizes the incoming and outcoming mass and energy flows for each of the processes assessed. Output streams considered as valuable products for the functional exergy efficiency are marked with a star (*).

3.3. Economic assessment

This work utilizes the BESP as the main indicator of the economic performance of the processes assessed. The BESP of each process is computed by setting their net present value (NPV) to zero, i.e., the BESP represents the electricity price at which the annualized revenues and costs of the plants are breakeven after a given lifetime of the plant. Thus, the economic assessment of the processes relies on the calculation of the NPV, which is computed from the discounted annual cash flows CF_i according to Eq. (14):

$$NPV = \sum_{i=1}^n \frac{CF_i}{(1+r)^i} \tag{14}$$

The cash flows are computed following a bottom-up approach that includes i) the calculation of the process equipment costs (for the units defined in each of the layouts in Section 3.1), ii) the addition of the installation and indirect costs, calculated according to [62] and iii) the fixed and variable plant operating costs. The cost of each process equipment is computed based on the known cost of a reference component of size S_0 and a scaling parameter f, through the expression defined in Eq. (15). Table 4 shows the cost functions (derived in M$) used for each of the process components included in the study. Note that the cost functions have been updated using the Chemical Engineering Plant Cost Index (CEPCI) and all costs are computed in USD2021.

$$C = C_0 \left(\frac{S}{S_0} \right)^f \tag{15}$$

In the charging reactor, the external input heat flow Q_{in} is assumed to be introduced through heat transfer surfaces of similar design as those of oxy-fuel circulating fluidized bed (CFB) furnaces, and therefore their capital cost function utilizes a reference cost of oxy-CFB furnaces extracted from [63]. Regarding the discharging reactor there are two different layouts: atmospheric vessels with heat extraction through steam generation (Rankine scheme) and adiabatic pressurized reactors (energy extracted through a Brayton scheme). Thus, cost data from a conventional CFB boiler is assumed for the former [63] while the cost of the latter is assumed to resemble such of a gas-solid FB gasifier [64] with a scaling factor of $f = 0.70$. As this equation is a function of the reactor volume (see Table 4), the sizing of these reactors is carried out following the procedure described in [68], with the mean particle residence times
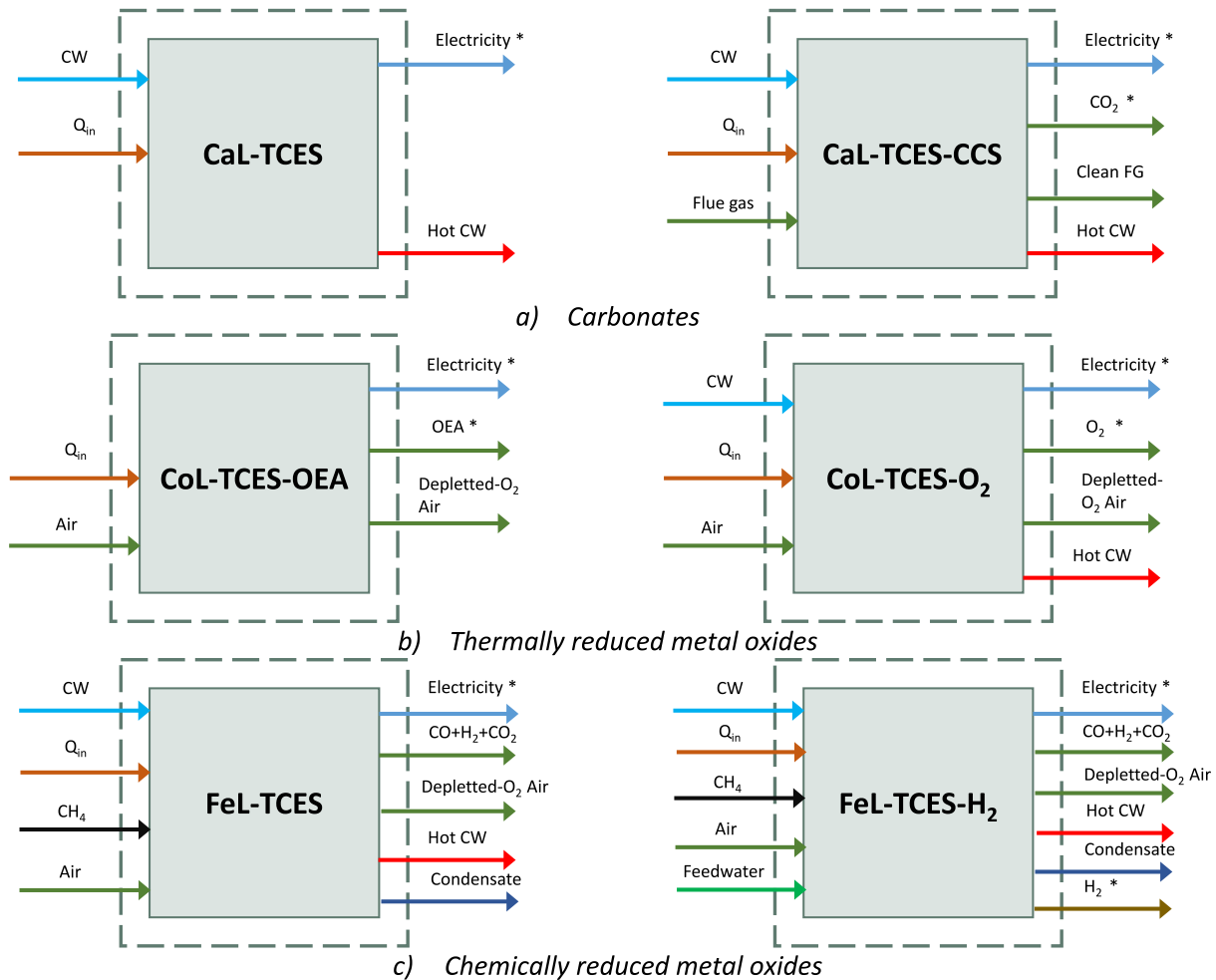
Fig. 8. Schematic of the input and output exergy streams considered for each of the processes. Streams marked with a (*) are considered as valuable output in the calculation of the functional efficiency (Eq. (14)). CW: cooling water. $\dot{Q}_{in}$: net renewable heat input. FG: flue gas.

listed in Table 5.

Due to a lack of available data, the cost of solids-solids heat exchangers is estimated to be double the cost of fluidized bed dryers [58], as they are designed on the principle of two bubbling fluidized beds. The gas-solids heat exchangers are sized as cyclones, as suggested by a previous publication [65] and following the method provided in [71]. Solids and gas storage tanks are in turn sized using the methodology suggested by Bayon et al. [40], whereas the water tanks are assumed to be standard cylindrical water vessels according to [72], with a total specific cost of 83 $/m$_{water}^3$ taken from [40]. Lastly, for the gas expanders and compressors the methodology provided by Michalski et al. [66] is followed to compute equivalent air mass flows, pressures and densities.

Table 6 lists the main economic parameters applied in this work. The CH$_4$ cost is estimated as an average of the cost between 2015 and 2020 [73] while the H$_2$ cost is taken from current production costs estimates [74]. The income derived from the carbon capture services provided by the *CaL-TCES-CCS* process is based on an estimation of the capture cost with a conventional post-combustion technology [75]. The CO$_2$ compression and storage steps are not included here as their costs are assumed to be transferred to the emitting industry and therefore not playing any role in the feasibility of the TCES plant. For the OEA and O$_2$ selling prices, the cost of membrane-based production has been considered, taking the most conservative end from the selling perspective, i.e., the lowest cost value [76,77]. Nonetheless, the impact of these prices on the computed results is evaluated in Section 4.2.1. Further, the cost of the renewable heat input is excluded from the baseline

assessment in order to provide a cost of the storage functionality of the processes, but a range is also considered in a parametric study in order to provide a picture of its magnitude in the total cost structure.

4. Results and discussion

This section presents and discusses the techno-economic performances of the six processes investigated. First, the technical analysis resulting from the mass, energy and exergy balances is presented in Section 4.1, followed by the economic assessment in Section 4.2 which includes a parametric study of the most important economic parameters.

4.1. Technical assessment

Fig. 9 shows a disclosure of the net distribution of exergy flows within each of the six investigated processes, with the inputs accounted as negative and the outputs as positive flows. The magnitude of the heat input is almost the same (it varies slightly depending on the charging temperature) over the six processes. The net chemical exergy input is lower for the case of *FeL-TCES-H$_2$* because of the chemical exergy output associated with the H$_2$ produced. Regarding thermally-charged systems, Co-based process layouts offer larger electricity production, which is attributed to the larger extent of conversion, reaction enthalpy (i.e., energy density) as well as the use of the Brayton cycle. The *FeL-TCES* and *FeL-TCES-H$_2$* processes (Fig. 9b, note the larger scale for the y-axis) have an additional input of chemical exergy attributed to the CH$_4$. The higher electricity production in these processes is a consequence of the fuel

Table 4

Capital cost functions (given in M$) of the process equipment included in the present study. Heat flows are in [MW$_{th}$], volumes in [m^3], diameters in [m], velocities in [m/s], areas in [m^2], pressures in [bar], electrical power in [kW] and mass flows in [kg s^{-1}].

Equipment	Cost function	Reference
Charging reactor	$C = 5.87 \cdot 10^2 \cdot \left(\dfrac{Q_{in}}{2514}\right)^{0.67}$	[63]
Atmospheric discharging reactor	$C = 5.60 \cdot 10^2 \cdot \left(\dfrac{Q_{out}}{1521}\right)^{0.67}$	[63]
Pressurized discharging reactor	$C = 1.16 \cdot \left(\dfrac{V_{reactor}}{42.41}\right)^{0.70}$	[64]
Gas-solids heat exchanger	$C = 3.98 \cdot 10^{-9} \cdot D_{cyc}^2 + 2.73 \cdot 10^{-6} \cdot D_{cyc} + 0.016$	[65]
Solids-solids heat exchanger	$C = 2 \cdot 3.5 \cdot 10^{-1} \cdot \left(\dfrac{D_b \cdot u_g}{2}\right)^{0.73}$	[58]
Gas-gas heat exchanger	$C = \left(2546.9 \cdot A_{HX}^{0.67} \cdot P_{gas}^{0.28}\right) \cdot 10^{-6}$	[66]
Cooler	$C = \left(2546.9 \cdot A_{HX}^{0.67} \cdot P_{fluid}^{0.28}\right) \cdot 10^{-6}$	[66]
Condenser	$C = \left(2546.9 \cdot A_{HX}^{0.67} \cdot P_{fluid}^{0.28}\right) \cdot 10^{-6}$	[66]
Solids storage	$C = V_{steel} \cdot C_{steel}$	[40]
Steam turbine	$C = 473 \cdot 10^{-6} \cdot \left(\dfrac{W_{turb}}{25}\right)^{0.67}$	[67]
Gas expander	$C = \dot{m}_{AE,E} \cdot \dfrac{392.2}{1 - \eta_{is}} \cdot \dfrac{p_{in}}{p_{AE,out}} \cdot ln\left(\dfrac{p_{in}}{p_{AE,out}}\right) \cdot [1 + exp(0.036 T_{in} - 65.66)]$	[66]
Gas compressor	$C = \dot{m}_{AE,E} \cdot \dfrac{47.1}{1 - \eta_{is}} \cdot \dfrac{p_{AE,out}}{p_{in}} \cdot ln\left(\dfrac{p_{AE,out}}{p_{in}}\right)$	[66]
Gas storage	$C = V_{steel} \cdot C_{steel}$	[40]
Steam generator	$C = 2.85 \cdot \left(\dfrac{\dot{m}_{steam}}{14}\right)^{0.35}$	[58]
Pump	$C = \left(\dfrac{W_{el}}{197}\right)^{0.60}$	[66]
Electric generator	$C = 84.5 \cdot 10^{-6} \cdot \left(W_{el} \cdot 10^3\right)^{0.95}$	[66]

Table 5

Mean particle residence time considered for the charging reactors where volume is required for the costing.

Reaction (process formulation)	Residence time of solids within the reactor [s]	Reference
$CaO + CO_2$ (*CaL-TCES*)	200	[69]
$CoO + O_2$ (*CoL-TCES-OEA* and *CoL-TCES-O$_2$*)	600	[55]
$FeO + H_2O$ (*FeL-TCES-H$_2$*)	1500	[70]

Table 6

Main input data and assumptions used for the economic assessment.

Parameter (unit)	Value	Reference
Plant lifetime, t (years)	20	[78]
Capacity factor (%)	100	[79]
Discount rate, r (%)	4.75	[78]
Limestone cost ($/t)	10–42	[79]
Cobalt oxide cost ($/t)	30,000	[80]
Iron oxide cost ($/t)	800	[11]
Oxygen-enriched air selling price ($/t)	5	[76]
Pure oxygen selling price ($/t)	67	[77]
Methane cost ($/t)	217	[73]
Hydrogen selling price ($/t)	1500	[74]
Carbon capture-derived income ($/t)	50	[75]
Renewable heat cost ($/kWt)	0–200	–
Cooling water cost ($/m^3)	0.03	[81]
Steel cost, C_{steel} ($/m^3)	5000	[80]

input and thus comparison with the thermally-charged processes can only be done in the light of the efficiencies. Fig. 10 displays the overall energy and exergy efficiencies (η_t and $\eta_{ex,t}$ respectively) and functional exergy efficiency, $\eta_{ex,f}$. As shown, the energy efficiency of the *CoL-TCES-OEA* layout is 45 % (the highest among the three *TCES-focused* layouts) The *CaL-TCES* and *FeL-TCES* layouts display energy efficiencies 26 % and 14 % lower than that of the *CoL-TCES-OEA* respectively, which

confirms that a higher energetic performance is strongly linked to higher extents of conversion and heat of reaction. Slightly lower values of efficiency will be obtained if temperature and pressure losses within each piece of equipment and pipeline are considered, however, the conclusions drawn from the comparison between processes would remain unaltered.

As seen in Fig. 9, the electricity production is lower in *by-product* layouts (i.e., the *CaL-TCES-CCS*, *CoL-TCES-O$_2$* and *FeL-TCES-H$_2$* layouts). This is due to i) the condensation of the steam used as an easy-to-separate carrier compound, and/or ii) the reduction in extent of reaction linked to the modified process conditions. Hence, the generation of a valuable by-product comes on the expense of the energetic performance of the process (7 and 6 %-points lower than the original layout for the Ca- and Co-based processes, respectively), except for the *FeL-TCES-H$_2$* case (where the energy efficiency is increased by 48 %-points as compared to the *FeL-TCES* layout). In fact, the *FeL-TCES-H$_2$* layout displays the best energetic and exergy performances when comparing all six processes, reaching a level comparable to that of the steam methane reforming process 75–85 % [82]. It is important to note that, as shown in the net physical exergy, $\dot{E}_{phys,net}$ (Fig. 9) and the total exergy efficiency, $\eta_{ex,tot}$ (Fig. 10), the production of valuable by-products involves an increase in heat production due to steam condensation. Accounting for the valorization of this produced heat would yield energy efficiencies surging up to >90 % [39].

Fig. 11 displays the net electricity production (i.e., negative values indicate a net consumption) in the charging and discharging sections for each of the processes. In the *CaL-TCES* and *CoL-TCES-OEA* layouts the charging side is a net electricity consumer, with most of this consumption being used for solids conveying. Consequently, the dispatchability ratios, rdisp of these processes are slightly larger than 1, i.e., the net electricity generated at the discharging section is higher than that of the whole process and therefore, these processes are considered fully dispatchable. Note that due to the increased use of steam in the charging side of *by-product* layouts (i.e., *CaL-TCES-CCS*, *CoL-TCES-O$_2$* and *FeL-TCES-H$_2$*) the share of non-dispatchable electricity generation increases,
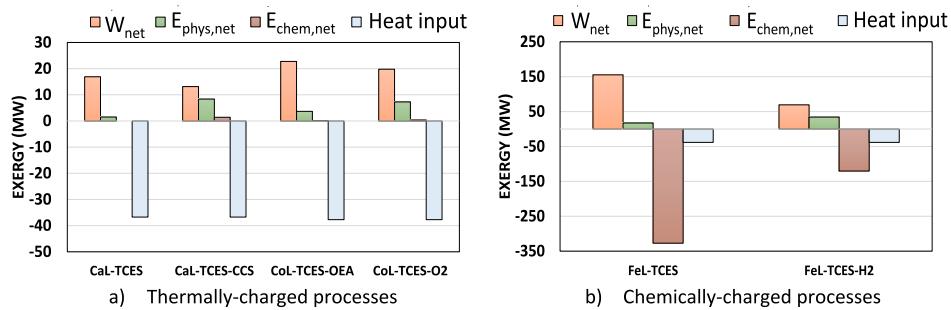
Fig. 9. Net (output-input) electricity production ($\dot{W}_{net}$), net physical exergy ($\dot{E}_{phys,net}$), net chemical exergy ($\dot{E}_{chem,net}$), and absolute heat input of each of the six processes assessed, grouped according to their charging input. Note that the scale of the y-axis is different between a) and b).
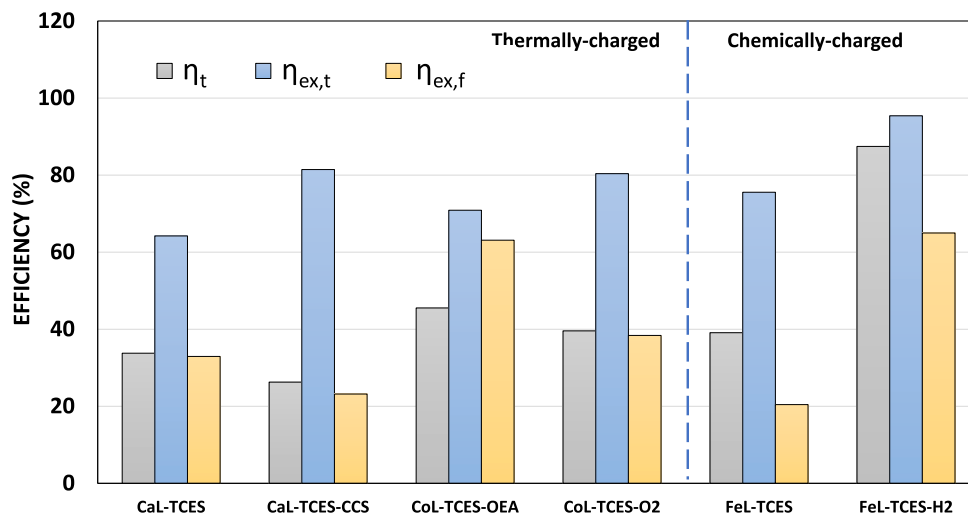

Fig. 10. Computed energy efficiency (η_t), total exergy efficiency ($\eta_{ex,t}$) and functional exergy efficiency ($\eta_{ex,f}$) of each of the six processes assessed, grouped according to their charging input.
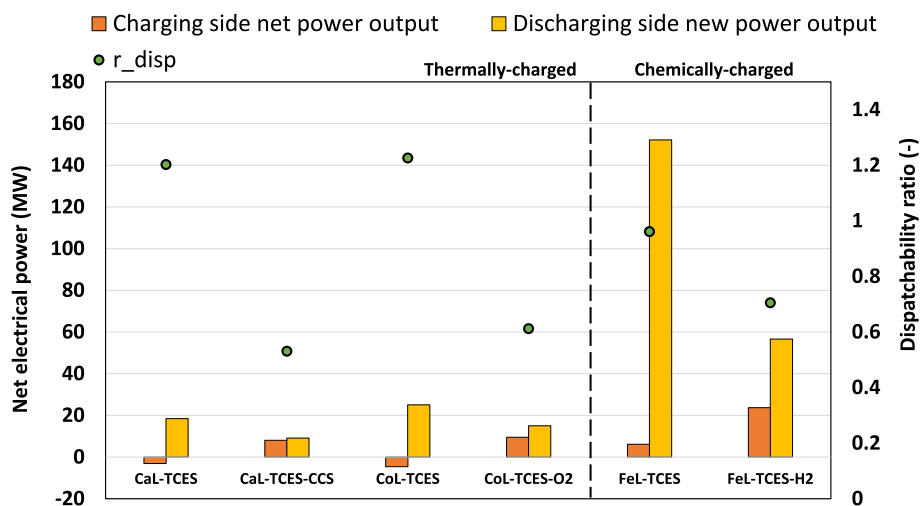

Fig. 11. Net electrical production of the charging and discharging sections and dispatchability ratio for each of the processes assessed.

therefore lowering the dispatchability (r_{disp} of 0.69, 0.76 and 0.83, respectively). This finding is in line with the reduction of the energy efficiency associated to the by-product production discussed above.

4.2. Economic assessment

An overview of the economic performances of the six processes

investigated is shown in Fig. 12, which includes the total cost, its breakdown and the BESP, for three different process sizes (in terms of Q_{in}, see Table 2). The total costs computed for the thermally-charged processes range between 106 and 230 M$ for the reference size of 100 MW (and within 66–494 M$ for the whole size range 50–250 MW). For any of the three sizes studied, *CaL-TCES* provides the lowest total plant cost and *CoL-TCES-OEA* the highest. The chemically-charged
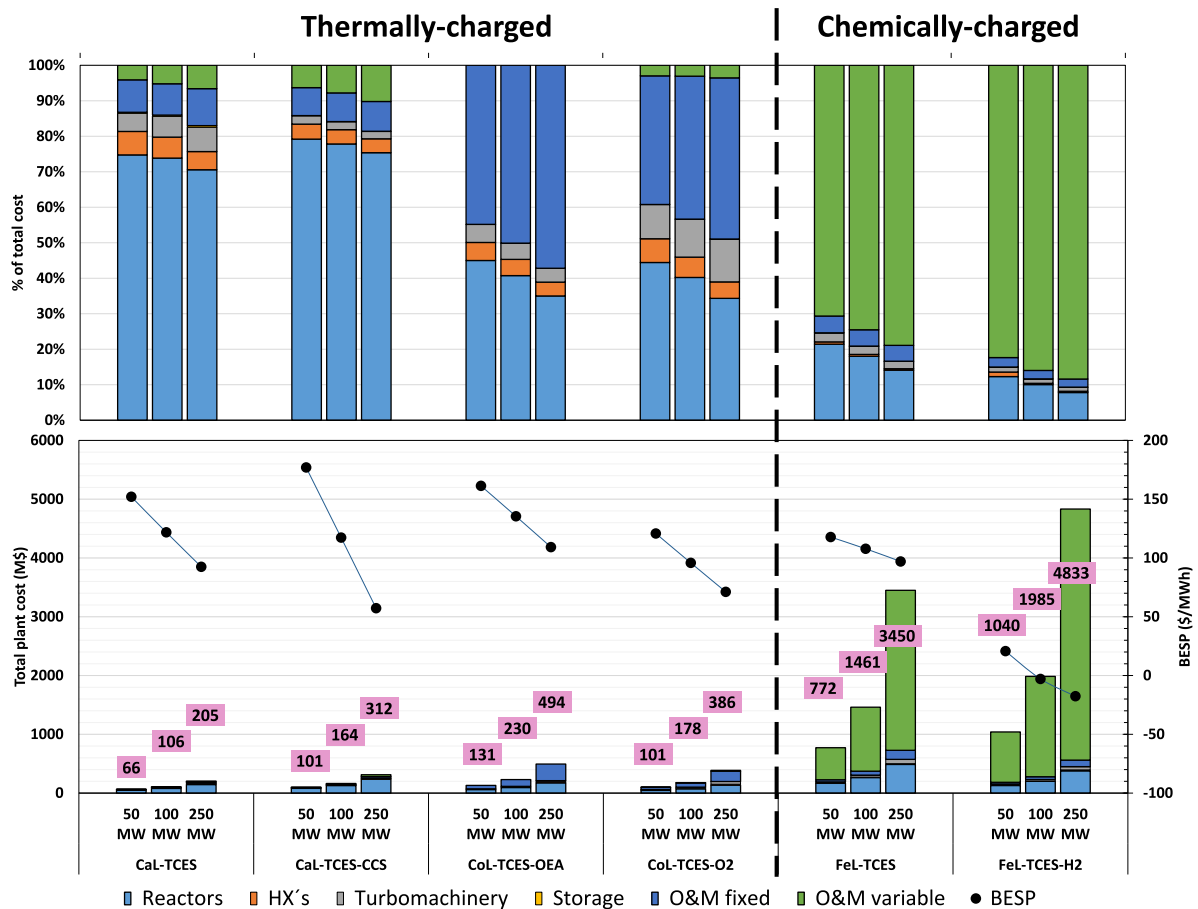
Fig. 12. Total plant cost (in M$), cost breakdown and BESP (in $/MWh) of each of the six processes assessed, grouped according to their charging input and computed for three different plant sizes. HX's: heat exchangers. O&M: operation and maintenance.

processes yield much (roughly 10 times) higher total plant cost than the thermally-charged, due to the much larger total energy flows to handle, see e.g. net energy produced in Fig. 11. It is important to note that while the *FeL-TCES-H₂* scheme involves an additional reactor as compared to the *FeL-TCES*, the share of cost due to reactors is smaller, as the air oxidator (discharging reactor) is much smaller and the adiabatic steam reactor (charger) represents a small cost due to the absence of heat transfer surfaces (see Table 4). Regarding the BESP, values for chemically-charged processes (20–118 $/MWh) lay in the same order of magnitude as for the thermally-charged (57–177 $/MWh) except for the two largest sizes of *FeL-TCES-H₂* (−2 and −17 $/MWh respectively).

For the CaL processes, the reactors account for the largest share (within 70–80 %) of the total cost regardless of the process size. It should be noted that the reactor cost includes the heat transfer surfaces for the charging reactor as well as the steam-related systems in the case of atmospheric discharging (see Table 4), i.e., *CaL-TCES-CCS*. The comparatively larger O&M variable cost in the *CaL-TCES-CCS* is attributed to the increase in cooling requirements necessary in the Rankine power cycle. Regarding the *CoL-based* processes, the O&M fixed costs (mainly associated to the purchase of inventory material) get roughly the same magnitudes as the reactor costs (in average 45 % for the *CoL-TCES-OEA* and 40 % for the *CoL-TCES-O₂* respectively), as previously highlighted by Bayon et al. [40]. Note also that the production of O₂ involves an added Rankine cycle that increases the turbomachinery cost and O&M variable costs as compared to the *CoL-TCES-OEA* layout. Lastly, the costs of the chemically-charged processes are largely dominated by the cost of the reducing agent (comprised within the O&M variable costs and representing 75 % (for *FeL-TCES*) and 85 % (*FeL-TCES-H₂*) of the total plant cost. The cost breakdown depicted in Fig. 12 denotes a decrease in the

share of CAPEX as the process size increases caused by the economy of scale ($f < 1$ in Eq. (15)). A very low cost is associated to the solids storage in all six processes due to i) the small sizes required, 500–1780 m³ for the thermally-charged and around 5000–7000 m³ for the chemically-charged processes (sizes calculated for the reference case of 100 MW capacity), as the storage time is set to 12 h and, ii) the fact that the storage is at ambient conditions and no insulation nor aeration is assumed to be required. This, together with the relatively low cost for the inventory of solids material in the CaL and FeL processes indicates that these could be deployed to cover much larger storage periods than the 12 h-period used as reference in this work, without strong alteration of the costs reported here. For the *CoL-TCES-OEA* and *CoL-TCES-O₂* processes, on other hand, a large increase in cost is expected for handling longer storage periods.

Overall, the *FeL-TCES-H₂* process presents by far the lowest BESP of the six processes assessed. For $\dot{Q}_{in}$ larger than 100 MW *FeL-TCES-H₂* displays negative BESP values, indicating that it would be a feasible option as a H₂-production facility, even without profiting from the electricity production. Nonetheless, chemically-charged (i.e., Fe-based) processes require enormous expenditures (most likely including further investments not considered in this work, e.g. increased grid capacity) compared to the thermally-charged. Regarding plant costs, the *FeL-TCES* presents the highest (up to 10 times larger than the thermally-charged processes), and with a BESP in the same order of magnitude. When comparing within thermally-charged processes, *CoL-TCES-O₂* offers the lowest BESP for the 50 and 100 MW scales while *CaL-TCES-CCS* is the most profitable option at the 250 MW scale.

Furthermore, the BESP is generally reduced in *by-product* layouts as compared to the simpler *TCES-focused* layouts, which confirms that

offering a side business is economically advantageous despite i) the drop in thermodynamic performance discussed in Section 4.1, and ii) the increased total cost (except for the Co-based processes, as the charging reactor in *CoL-TCES-O₂* is much smaller than that in *CoL-TCES-OEA* due to the use of a share of the heat input for the production of steam). The increased economic performance in terms of BESP is in average (i.e., considering all the sizes studies) 5 % for the CaL processes, 29 % for the CoL and >99 % for the FeL (for which the BESP becomes negative, i.e., the *FeL-TCES-H₂* would be profitable as a H₂-generation process without the need to sell dispatchable electricity). Note that the benefit of implementing *CaL-TCES-CCS* as compared to *CaL-TCES* is more noticeable at larger process sizes: 38 % BESP reduction for the 250 MW size, whereas for the 100 MW the BESP barely changes and for 50 MW the implementation of side-business increases the BESP. The main reason for this is the fact that the *CaL-TCES-CCS* layout is formulated with an atmospheric discharging reactor that includes a steam-generation system, which is more expensive than the adiabatic carbonator of the CaL-TCES. With an increasing process size, the relative cost of the reactor is decreased (favored by the economy of scale) while the profit related to the CO₂-capture services increases linearly. On the contrary, the *FeL-TCES* process shows the lowest BESP reductions with increased size, which indicates that the CAPEX is not playing as big role as compared to the linear O&M costs (largely dominated by the CH₄ consumption). Looking at the TCES-focused processes, the results make evident that despite the favorable technical performance (i.e., higher energy efficiency and dispatchability ratio) of *CoL-TCES-OEA*, both the Ca-based and Fe-based (i.e., *CaL-TCES* and *FeL-TCES*) show a better economic performance, due to the significantly lower cost of the solids materials.

It should be noted that the computation of the BESP as an economic assessment metric implies valuing equally the dispatchable and non-dispatchable electricity production. In reality, these will have different values (as the dispatchable electricity could be intentionally sold in periods of high electricity prices), which would reduce the BESP of the processes with larger r_{disp} (i.e., *CaL-TCES*, *CoL-TCES-OEA* and *FeL-TCES*, see Fig. 11). Considering that the main purpose of the present work is to compare the performance of the different processes, a capacity factor of 100 % (ideal) was chosen. This assumption simplifies the comparison (by reducing the degrees of freedom), but naturally affects the resulting capacity of the reactors and storages, as lower capacity factors would result in higher costs and different BESP values.

The computed BESP values calculated in this work can be contextualized by comparison with previously reported cost values of similar processes. For example, Muto et al. [83] computed a levelized cost of electricity (LCOE) of 56–59 $/MWhₑ for a *CaL-TCES* process using a synthetic sorbent. That is comparable to the *CaL-TCES* cost computed here (92–152 $/MWh), taking into account that only one reactor was considered by Muto et al. Among the investigations that evaluate the feasibility of the CaL process as a CO₂-capture process to be implemented in existing power stations, the study by Hanak and Manovic [79] included a comprehensive weighing of uncertainties and parametric variations. Their conclusion was that the production of electricity with CaL-CCS in place would have a cost within the range 50–150 $/MWhₑ, which is in line with our results.

The results presented here are aligned with several aspects highlighted in the economic analysis of different large-scale gas-solid TCES systems carried out by Bayon et al. [40] (who however disregarded the reactor costs, found in this work to play a crucial role): i) the cost of CoL processes is largely affected by the material cost and therefore not feasible for implementation in long-term storage; ii) despite the CaL having a lower energy efficiency than CoL, it results more attractive for TCES applications due to the very low material cost; and iii) the large economic potential of FeL when utilizing a reducing agent due to its high energetic efficiency. Regarding the last one, the range of BESP values calculated here (97–117 $/MWh for the *FeL-TCES*) is similar to the 80–120 $/MWh reported by Porrazzo et al. [84] for a CH₄-based CLC power plant (i.e., without storage) and can be compared to the LCOE of

conventional natural gas power plants (56 $/MWhₑ in 2019 according to [85]).

4.2.1. Parametric study

The low TRL of the processes assessed in this work entails large uncertainties on the costs reported. Thus, a parametric study is conducted to examine how BESP of the different processes reacts to the variation of those parameters for which uncertainty is relatively large in terms of their role in the cost structure. Although the specific parameters included in the study differ among processes, the general aspects assessed here are: i) the cost related to the generation of the renewable high-temperature heat input, ii) the cost of cooling water, iii) the cost of solid material, the iv) the selling price of the by-product, and v) the cost of the reducing agent (for chemically-charged processes). The sensitivity study of BESP is presented in Fig. 13 and takes as base case the values presented in Section 3.3 (Table 6).

The cost of the renewable heat generation, disregarded in the results reported above, is varied up to 200 $/kW (the average cost for high-temperature solar receivers [86]). Such variation yields its highest impact for *CaL-TCES*, (BESP increases 28 %, see Fig. 13a), and the lowest impact for *FeL-TCES* (BESP increases 2 %, see Fig. 13e). This goes in line with the results shown in Fig. 12 that indicate that while the *CaL-TCES* cost structure is largely driven by the CAPEX, the *FeL-TCES* is driven by the OPEX. The increased BESP for the thermally-charged processes is in line with the figures predicted in [87] that estimated an added cost on the electricity production of 20–70 $/MWh when accounting for high-temperature CSP equipment.

The assumed cost for cooling water is tightly linked to the source available on-site. While the present work assumes an open-loop cooling circuit (i.e., water is taken from and returned to a nearby river or sea), a more CAPEX-intensive option (typically implying cooling towers) is required when a cooling water source is not available. As displayed in Fig. 13, an increase of 50 % in the cost of cooling water yields an average ± 2.5 % variation on the computed BESP for processes with a Rankine power cycle.

The impact of the cost of solids material on the BESP is well in line with the share of the total investment cost that corresponds to the material (plotted in Fig. 12). *CoL-TCES-OEA* and *CoL-TCES-O₂* processes (Fig. 13c and d) are found to be the most sensitive to changes in solids material cost, with their BESP increasing by 14 % when the Co oxide cost is increased by 50 %. On the contrary, Ca - and Fe- based process performances barely notice (−0.12 % − +0.5 % and −0.36 % − +0.7 % respectively) a ten-times increase in material cost. It is important to notice that while the make-up flow of fresh material has not been included in the present work, these results based on the solids inventory provide a rough indication of the impact such aspect would have if accounted.

Results in Fig. 13 show that the byproduct processes are largely sensitive to the assumed selling price of the by-product/service provided. For example, the *CaL-TCES-CCS* process has a negative BESP of −8 $/MWh when a carbon tax of 100 $/t is assumed (a realistic value in Europe as of 2023 [88]). This indicates that, as it was highlighted in a previous study [41], under such conditions the *CaL-TCES-CCS* process would be profitable as a carbon capture unit regardless of the electricity produced. The BESP of the *CoL-TCES-O₂* process changes by ±13–18 % if the selling price of O₂ is varied to match a more optimistic estimate of the production cost of O₂ through current commercial technologies (i.e., cryogenic separation or different types of membranes [89]). For *FeL-TCES-H₂* the BESP increases up to 99 $/MWh (i.e., similar than the TCES-focused process layout, *FeL-TCES*) for H₂ selling prices dropping to 1000 $/t (a representative value for fossil H₂ with very low natural gas prices [90]). On the other hand, if the hydrogen H₂ price is assumed to be 4000 $/t [74], the profitability of the process would reach a BESP of −509 $/MWh.

Lastly, the need of a reducing agent for the charging makes the chemically-charged processes very sensitive to its cost. In the results
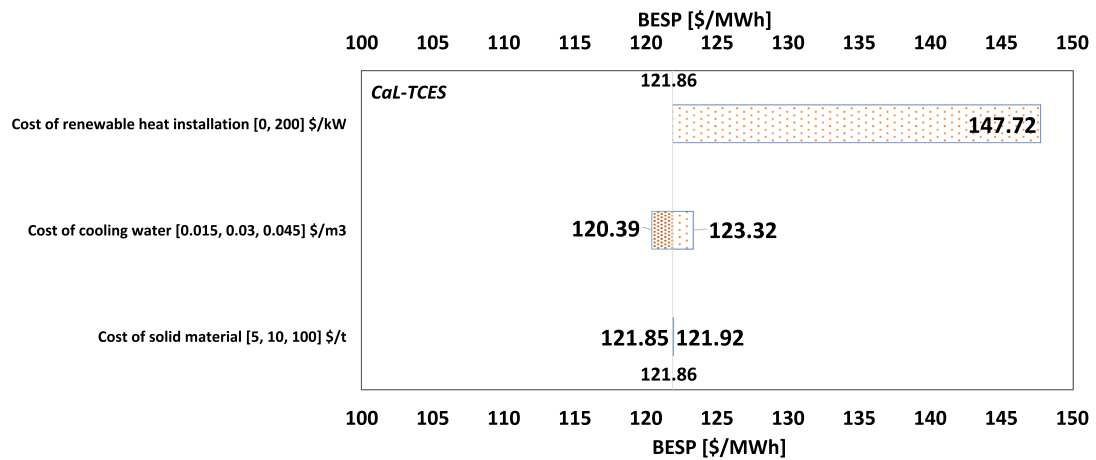
a) BESP variations on the *CaL-TCES* process when the renewable heat cost, cooling water cost and solid material cost are varied independently.
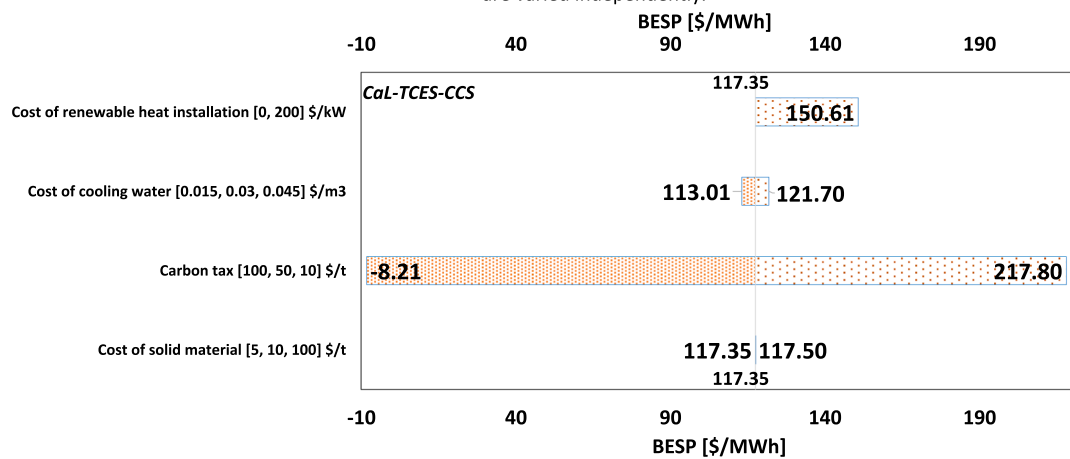
b) BESP variations on the *CaL-TCES-CCS* process when the renewable heat cost, cooling water cost, carbon tax and solid material cost are varied independently.
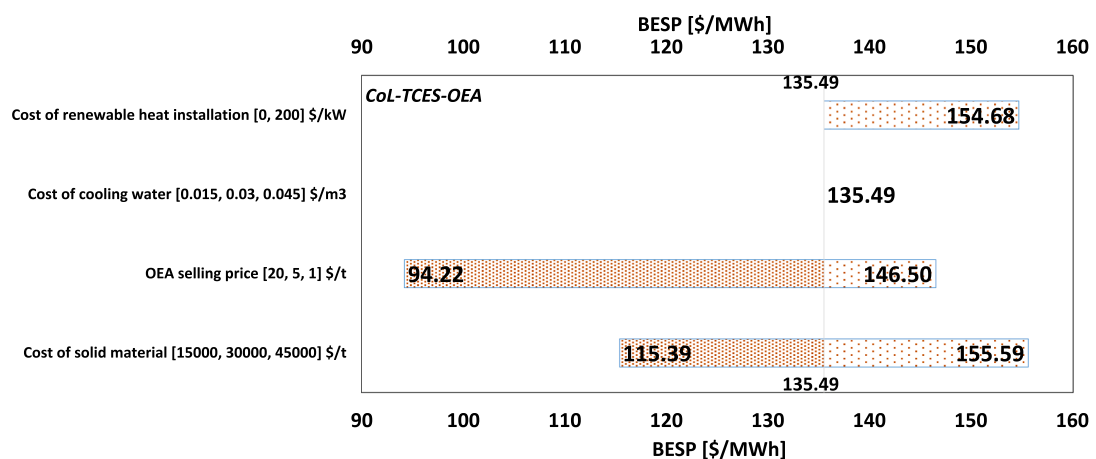
c) BESP variations on the *CoL-TCES-OEA* process when the renewable heat cost, cooling water cost, OEA selling price and solid material cost are varied independently.

Fig. 13. Results from the parametric study for each of the six processes assessed. a) BESP variations on the *CaL-TCES* process when the renewable heat cost, cooling water cost and solid material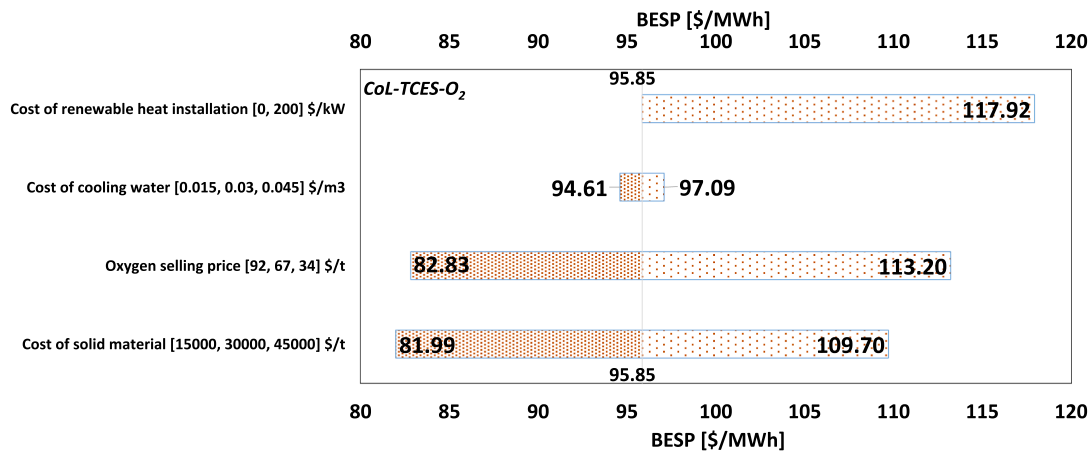 cost are varied independently. b) BESP variations on the *CaL-TCES-CCS* process when the renewable heat cost, cooling water cost, carbon tax and soli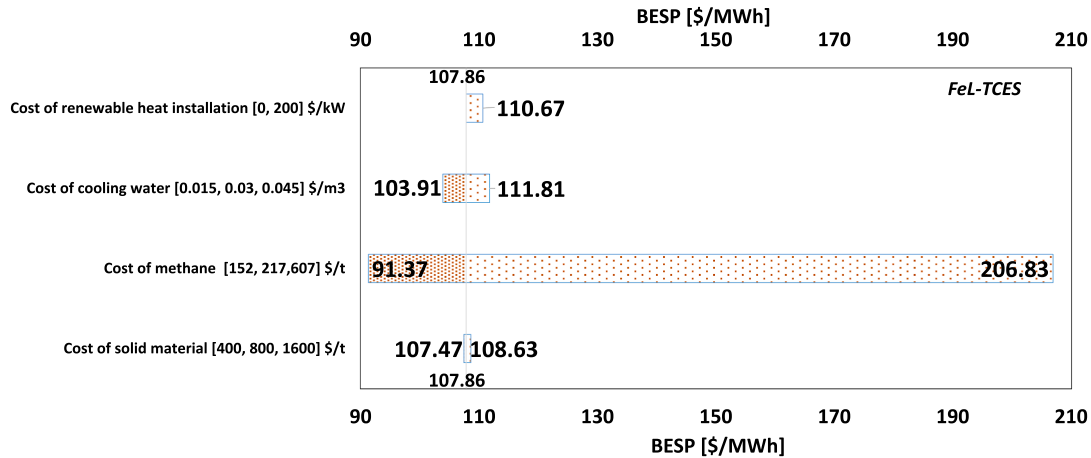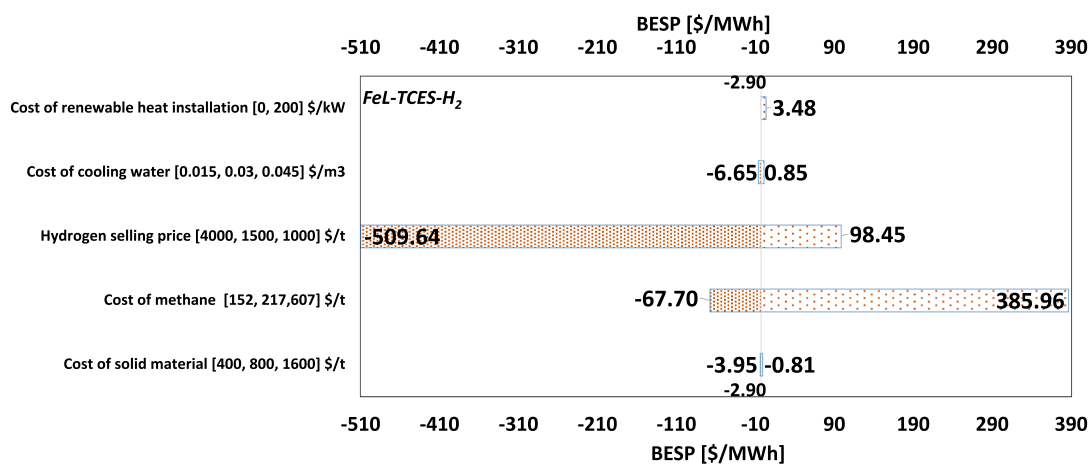d material cost are varied independently. c) BESP variations on the *CoL-TCES-OEA* process when the renewable heat cost, cooling water cost, OEA selling price and solid material cost are varied independently. d) BESP variations on the *CoL-TCES-O₂* process when the renewable heat cost, cooling water cost, oxygen selling price and solid material cost are varied independently. e) BESP variations on the *FeL-TCES* process when the renewable heat cost, cooling water cost, methane cost and solid material cost are varied independently. f) BESP variations on the *FeL-TCES-H₂* process when the renewable heat cost, cooling water cost, hydrogen selling price, methane cost and solid material cost are varied independently.

d) BESP variations on the *CoL-TCES-O₂* process when the renewable heat cost, cooling water cost, oxygen selling price and solid material cost are varied independently.

e) BESP variations on the *FeL-TCES* process when the renewable heat cost, cooling water cost, methane cost and solid material cost are varied independently.

f) BESP variations on the *FeL-TCES-H₂* process when the renewable heat cost, cooling water cost, hydrogen selling price, methane cost and solid material cost are varied independently.

Fig. 13. (*continued*).

displayed in Fig. 13 the base cost assumed for CH_4 (217 $/t) has been varied within 152–607 $/ton. It can be observed that for the higher value, which represents the possibility of using biomethane [91], the BESP is increased by 92 % in the *FeL-TCES* case and by 13,400 % in the *FeL-TCES-H₂* (i.e., to 206 and 385 $/MWh respectively), once again making the *FeL-TCES-H₂* less profitable than the *FeL-TCES*.

Based on parametric study conducted, several conclusions can be extracted. Firstly, that the *CaL-TCES* cost reported here is the most robust to the variations considered in the study. Secondly, that although the economic performances of the two Co-based processes are affected by the material cost and the by-product selling price, the BESP remains within the same order of magnitude (80–155 $/MWh for all cases

studied). Lastly, the study has shown that the best-performing process, *FeL-TCES-H$_2$* is extremely sensitive to the set of assumptions considered, becoming a less profitable option than the simpler *FeL-TCES* process for high CH$_4$ and low H$_2$ prices.

5. Conclusions

This work evaluates the techno-economic feasibility of the previously identified prime candidates for thermochemical energy storage (carbonates, thermally-reduced and chemically-reduced metal oxides) when deployed for high-temperature applications at large-scale. The cost structures for the processes considered differ significantly: while the cost of carbonate processes (Ca-based) is largely driven by the cost of the reactors, the influence of the solid material governs the feasibility of thermally-reduced processes (Co-based). Alternatively, chemically-charged process layouts (Fe-based) exhibit very large O&M costs related to the need for a reducing agent. In fact, due to the large amounts of reducing agent involved, the use of chemically-charged processes yield costs up to 10 times larger than for thermally-charged systems, but also the by far lowest a much lower BESP if co-generation of H$_2$ is implemented in the discharge section of the Fe-based process. The results show that despite the more favorable technical performance of the Co-based processes (with electrical efficiency of 45 % and dispatchability ratio of 1), the largest-sized Ca-based process with integrated CCS yields the best economic performance among the low cost (i.e., the thermally-charged) layouts considered, owing to the use of inexpensive material.

This study represents a first attempt towards linking thermodynamic conditions with large-scale process performance, and it reveals the need for further research in several areas. While the cost of the FB reactors is found to be a crucial element in most of the investigated cases, there is little knowledge regarding the design of large-scale solar FB reactors and their cost structures. Similarly, optimizing the process design and operation so as to maximize the performance and flexibility would largely enhance the computed costs. Lastly, given the expected variations of electricity prices as the shares of VRE in the grid increase, the dispatchability of electricity will gain added value. Thus, smart dispatching (specially of the processes with high dispatchability ratio) would yield improvements in the economic feasibility features reported herein.

Nomenclature

Abbreviations

ARx	air reactor
BESP	breakeven electricity selling price
CaL	calcium looping
CCS	carbon capture and storage
CLC	chemical looping combustion
CoL	cobalt looping
CSP	concentrated solar power
FeL	iron looping
FB	fluidized bed
FG	flue gas
G-G	gas-gas
HX	heat exchanger
NPV	net present value
O&M	operation and maintenance
S-G	solids-gas
S-S	solids-solids
SRx	steam reactor
TCES	thermochemical energy storage
VRE	variable renewable energy

Variables

A_{HX}	heat exchanger area [m^2]
C	cost [M\$]
C_0	reference cost [M\$]
CF_i	cash flow in year I [M\$ year^{-1}]
D_b	bed diameter [m]
D_{cyc}	cyclone diameter [m]
$\dot{E}_{chem}$	chemical exergy flow [MW]
$\dot{E}_{tot}$	total exergy flow [MW]
$\dot{E}_{phys}$	physical exergy flow [MW]
$E_{0,i}$	standard chemical exergy of the component I [J kg^{-1}]
f	scaling factor
F_{ch}	charging reactor mass flow rate [kg s^{-1}]
F_{disch}	discharge reactor mass flow rate [kg s^{-1}]
h_i	specific enthalpy of component I [J kg^{-1}]
$h_{0,i}$	specific enthalpy of component i at the dead state conditions [J kg^{-1}]
$I_{destroyed}$	irreversibility generated [MW]
$\dot{m}_{AE,E}$	equivalent air mass flow [kg s^{-1}]
$\dot{m}_{steam}$	mass flow rate of steam [kg s^{-1}]
$\frac{p_0}{p_{00}}$	partial pressure at the dead state conditions [−]
$p_{AE,out}$	equivalent air pressure outlet [bar]
p_{fluid}	fluid pressure [bar]
p_{in}	inlet pressure [bar]
$\dot{Q}_{chem,in}$	chemical energy input [MW]
$\dot{Q}_{chem,out}$	chemical energy output [MW]
$\dot{Q}_{in}$	net heat input [MW]
Q_{out}	heat output [MW]
r	discount rate [%]
r_{disp}:	dispatchability ratio [−].
S	sizing variable
t_{ch}	charging time [h]
t_{disch}	discharging time [h]
T_{ch}	charging reactor temperature [K]
T_0	dead state temperature [K]
S_0	reference sizing variable
s_i	specific entropy of component I [J kg^{-1}]
$s_{0,i}$	specific entropy of component I at the dead state conditions [J kg^{-1}]
u_g	gas velocity [m/s]
$V_{reactor}$	reactor volume [m^3]
V_{steel}	volume of steel [m^3]
W_{el}	turbomachinery power consumption [kW]
$\dot{W}_{net}$	net power [MW]
x_i	mass fraction of component I [−]
$\eta_{ex,f}$	functional exergy efficiency [%]
$\eta_{ex,t}$	total exergy efficiency [%]
η_{is}	isentropic efficiency [%]

CRediT authorship contribution statement

Guillermo Martinez Castilla: Writing – original draft, Visualization, Software, Methodology, Conceptualization. **Diana Carolina Guío-Pérez:** Writing – review & editing, Visualization, Methodology, Conceptualization. **Filip Johnsson:** Writing – review & editing, Supervision, Conceptualization. **David Pallarès:** Writing – review & editing, Supervision, Conceptualization.

Declaration of competing interest

The authors declare that they have no known competing financial interests or personal relationships that could have appeared to influence the work reported in this paper.

Data availability

No data was used for the research described in the article.

Appendix A. Supplementary data

Supplementary data to this article can be found online at https://doi.org/10.1016/j.est.2024.113944.

References

[1] International Renewable Energy Agency, IRENA (2019), Global energy transformation: a roadmap to 2050 [Online]. Available: https://www.irena.org/publications/2019/Apr/Global-energy-transformation-A-roadmap-to-2050-2019Edition, 2019.

[2] International Energy Agency, World energy outlook 2021: part of the world energy outlook, Paris, [Online]. Available: https://www.iea.org/reports/world-energy-outlook-2021, 2021.

[3] P.E. Bett, H.E. Thornton, The climatological relationships between wind and solar energy supply in Britain, Renew. Energy 87 (2016) 96–110, https://doi.org/10.1016/j.renene.2015.10.006.

[4] B.M.S. Hodge, et al., Addressing technical challenges in 100% variable inverter-based renewable energy power systems, Wiley Interdiscip. Rev. Energy Environ. 9 (5) (2020) 1–19, https://doi.org/10.1002/wene.376.

[5] L. Göransson, F. Johnsson, A comparison of variation management strategies for wind power integration in different electricity system contexts, Wind Energy 21 (10) (2018) 837–854, https://doi.org/10.1002/we.2198.

[6] S. Rehman, L.M. Al-Hadhrami, M.M. Alam, Pumped hydro energy storage system: a technological review, Renew. Sust. Energ. Rev. 44 (2015) 586–598, https://doi.org/10.1016/j.rser.2014.12.040.

[7] G. Venkataramani, P. Parankusam, V. Ramalingam, J. Wang, A review on compressed air energy storage – a pathway for smart grid and polygeneration, Renew. Sust. Energ. Rev. 62 (2016) 895–907, https://doi.org/10.1016/j.rser.2016.05.002.

[8] F. Díaz-González, A. Sumper, O. Gomis-Bellmunt, R. Villafáfila-Robles, A review of energy storage technologies for wind power applications, Renew. Sust. Energ. Rev. 16 (4) (2012) 2154–2171, https://doi.org/10.1016/j.rser.2012.01.029.

[9] A. Gil, et al., State of the art on high temperature thermal energy storage for power generation. Part 1-concepts, materials and modellization, Renew. Sust. Energ. Rev. 14 (1) (2010) 31–55, https://doi.org/10.1016/j.rser.2009.07.035.

[10] P. Pardo, A. Deydier, Z. Anxionnaz-Minvielle, S. Rougé, M. Cabassud, P. Cognet, A review on high temperature thermochemical heat energy storage, Renew. Sust. Energ. Rev. 32 (2014) 591–610, https://doi.org/10.1016/j.rser.2013.12.014.

[11] S. Wu, C. Zhou, E. Doroodchi, R. Nellore, B. Moghtaderi, A review on high-temperature thermochemical energy storage based on metal oxides redox cycle, Energy Convers. Manag. 168 (March) (2018) 421–453, https://doi.org/10.1016/j.enconman.2018.05.017.

[12] K.E. N'Tsoukpoe, H. Liu, N. Le Pierrès, L. Luo, A review on long-term sorption solar energy storage, Renew. Sust. Energ. Rev. 13 (9) (2009) 2385–2396, https://doi.org/10.1016/j.rser.2009.05.008.

[13] C. Ortiz, J. Manuel Valverde, R. Chacartegui, L.A. Pérez-Maqueda, P. Gimenez-Gavarrell, Scaling-up the calcium-looping process for CO$_2$ capture and energy storage, Kona Powder Part. J. no. March (2021) 1–20, https://doi.org/10.14356/kona.2021005.

[14] A.J. Carrillo, J. González-Aguilar, M. Romero, J.M. Coronado, Solar energy on demand: a review on high temperature thermochemical heat storage systems and materials, Chem. Rev. 119 (7) (2019) 4777–4816, https://doi.org/10.1021/acs.chemrev.8b00315.

[15] L. André, S. Abanades, G. Flamant, Screening of thermochemical systems based on solid-gas reversible reactions for high temperature solar thermal energy storage, Renew. Sust. Energ. Rev. 64 (2016) 703–715, https://doi.org/10.1016/j.rser.2016.06.043.

[16] Y. Yan, K. Wang, P.T. Clough, E.J. Anthony, Developments in calcium/chemical looping and metal oxide redox cycles for high-temperature thermochemical energy storage: a review, Fuel Process. Technol. 199 (November 2019) (2020) 106280, https://doi.org/10.1016/j.fuproc.2019.106280.

[17] F. Scala, Fluidized Bed Technologies for Near-Zero Emission Combustion and Gasification, Woodhead Publishing Series, Cambridge, 2013.

[18] J.L. Schenk, Recent status of fluidized bed technologies for producing iron input materials for steelmaking, Particuology 9 (1) (2011) 14–23, https://doi.org/10.1016/j.partic.2010.08.011.

[19] Socratces Project. https://socratces.eu/, 2021.

[20] X.C. Mi, A. Fujinawa, J.M. Bergthorson, A quantitative analysis of the ignition characteristics of fine iron particles, Combust. Flame 240 (2022) 112011, https://doi.org/10.1016/j.combustflame.2022.112011.

[21] D.N. Harries, M. Paskevicius, D.A. Sheppard, T.E.C. Price, C.E. Buckley, Concentrating solar thermal heat storage using metal hydrides, Proc. IEEE 100 (2) (2012) 539–549, https://doi.org/10.1109/JPROC.2011.2158509.

[22] H.B. Dizaji, H. Hosseini, A review of material screening in pure and mixed-metal oxide thermochemical energy storage (TCES) systems for concentrated solar power (CSP) applications, Renew. Sust. Energ. Rev. 98 (July) (2018) 9–26, https://doi.org/10.1016/j.rser.2018.09.004.

[23] C. Ortiz, J.M. Valverde, R. Chacartegui, L.A. Perez-Maqueda, P. Giménez, The calcium-looping (CaCO$_3$/CaO) process for thermochemical energy storage in concentrating solar power plants, Renew. Sust. Energ. Rev. 113 (July) (2019) 109252, https://doi.org/10.1016/j.rser.2019.109252.

[24] J. Ylätalo, J. Ritvanen, T. Tynjälä, T. Hyppänen, Model based scale-up study of the calcium looping process, Fuel 115 (2014) 329–337, https://doi.org/10.1016/j.fuel.2013.07.036.

[25] B. Arias, et al., Operating experience in la Pereda 1.7 MWth calcium looping pilot, Energy Procedia 114 (2017) 149–157, https://doi.org/10.1016/j.egypro.2017.03.1157.

[26] B. Wong, L. Brown, F. Schaube, R. Tamme, S.C., Oxide based thermochemical heat storage, in: SolarPACES, 2010.

[27] C. Agrafiotis, M. Roeb, M. Schmücker, C. Sattler, Exploitation of thermochemical cycles based on solid oxide redox systems for thermochemical storage of solar heat. Part 1: testing of cobalt oxide-based powders, Sol. Energy 102 (2014) 189–211, https://doi.org/10.1016/j.solener.2013.12.032.

[28] C. Agrafiotis, S. Tescari, M. Roeb, M. Schmücker, C. Sattler, Exploitation of thermochemical cycles based on solid oxide redox systems for thermochemical storage of solar heat. Part 3: cobalt oxide monolithic porous structures as integrated thermochemical reactors/heat exchangers, Sol. Energy 114 (2015) 459–475, https://doi.org/10.1016/j.solener.2014.12.037.

[29] G. Karagiannakis, C. Pagkoura, A. Zygogianni, S. Lorentzou, A.G. Konstandopoulos, Monolithic ceramic redox materials for thermochemical heat storage applications in CSP plants, Energy Procedia 49 (2014) 820–829, https://doi.org/10.1016/j.egypro.2014.03.089.

[30] S. Padula, C. Tregambi, R. Solimene, R. Chirone, M. Troiano, P. Salatino, A novel fluidized bed 'thermochemical battery' for energy storage in concentrated solar thermal technologies, Energy Convers. Manag. 236 (2021) 113994, https://doi.org/10.1016/j.enconman.2021.113994.

[31] M. Alvarez Rivero, D. Rodrigues, C.I.C. Pinheiro, J.P. Cardoso, L.F. Mendes, Solid-gas reactors driven by concentrated solar energy with potential application to calcium looping: a comparative review, Renew. Sust. Energ. Rev. 158 (January) (2022) 112048, https://doi.org/10.1016/j.rser.2021.112048.

[32] Vatenfall, First power-to-heat plant in Hamburg to convert wind energy into heat. https://group.vattenfall.com/press-and-media/newsroom/2019/first-power-to-heat-plant-in-hamburg-to-convert-wind-energy-into-heat, February 15, 2019.

[33] P. Fenell, B. Anthony, Calcium and Chemical Looping Technology for Power Generation and Carbon Dioxide (CO$_2$) Capture vol. 1 (82), Woodhead Publoshing Series, Cambridge, 2015.

[34] R. Chacartegui, A. Alovisio, C. Ortiz, J.M. Valverde, V. Verda, J.A. Becerra, Thermochemical energy storage of concentrated solar power by integration of the calcium looping process and a CO$_2$ power cycle, Appl. Energy 173 (2016) 589–605, https://doi.org/10.1016/j.apenergy.2016.04.053.

[35] S. Pascual, P. Lisbona, L.M. Romeo, Operation maps in calcium looping thermochemical energy storage for concentrating solar power plants, J. Energy Storage 55 (PD) (2022) 105771, https://doi.org/10.1016/j.est.2022.105771.

[36] D. Rodrigues, C.I.C. Pinheiro, R.M. Filipe, L.F. Mendes, H.A. Matos, Optimization of an improved calcium-looping process for thermochemical energy storage in concentrating solar power plants, J. Energy Storage 72 (PB) (2023) 108199, https://doi.org/10.1016/j.est.2023.108199.

[37] S. Wu, C. Zhou, E. Doroodchi, B. Moghtaderi, Thermodynamic analysis of a novel hybrid thermochemical-compressed air energy storage system powered by wind, solar and/or off-peak electricity, Energy Convers. Manag. 180 (December 2018) (2019) 1268–1280, https://doi.org/10.1016/j.enconman.2018.11.063.

[38] A.J. Schrader, A.P. Muroyama, P.G. Loutzenhiser, Solar electricity via an Air Brayton cycle with an integrated two-step thermochemical cycle for heat storage based on Co$_3$O$_4$/CoO redox reactions: thermodynamic analysis, Sol. Energy 118 (2015) 485–495, https://doi.org/10.1016/j.solener.2015.05.045.

[39] D.C. Guio-Perez, G. Martinez Castilla, D. Pallares, F. Johnsson, H. Thunman, Thermochemical energy storage with integrated district heat production – a case study of Sweden, Energies 16 (1155) (2023), https://doi.org/10.3390/en16031155.

[40] A. Bayon, et al., Techno-economic assessment of solid-gas thermochemical energy storage systems for solar thermal power applications, Energy 149 (2018) 473–484, https://doi.org/10.1016/j.energy.2017.11.084.

[41] G. Martinez Castilla, D.C. Guio-Perez, S. Papadokonstantakis, D. Pallarès, F. Johnsson, Techno-economic assessment of calcium looping for thermochemical energy storage with CO$_2$ capture, Energies 14 (11) (2021) 3211.

[42] A. Lyngfelt, Chemical looping combustion: status and development challenges, Energy Fuel 34 (2020) 9077–9093, https://doi.org/10.1021/acs.energyfuels.0c01454.

[43] S. Abanades, P. Charvin, G. Flamant, P. Neveu, Screening of water-splitting thermochemical cycles potentially attractive for hydrogen production by concentrated solar energy, Energy 31 (14) (2006) 2805–2822, https://doi.org/10.1016/j.energy.2005.11.002.

[44] C. Agrafiotis, M. Roeb, C. Sattler, A review on solar thermal syngas production via redox pair-based water/carbon dioxide splitting thermochemical cycles, Renew. Sust. Energ. Rev. 42 (2015) 254–285, https://doi.org/10.1016/j.rser.2014.09.039.

[45] US Department of Energy, Thermochemical Heat Storage for Concentrated Solar Power. Thermochemical System Reactor Design for Thermal Energy Storage, 2011, https://doi.org/10.2172/1039304.

[46] S. Chuayboon, S. Abanades, An overview of solar decarbonization processes, reacting oxide materials, and thermochemical reactors for hydrogen and syngas production, Int. J. Hydrog. Energy 45 (48) (2020) 25783–25810, https://doi.org/10.1016/j.ijhydene.2020.04.098.

[47] M. Jafarian, M. Arjomandi, G.J. Nathan, A hybrid solar and chemical looping combustion system for solar thermal energy storage, Appl. Energy 103 (2013) 671–678, https://doi.org/10.1016/j.apenergy.2012.10.033.

[48] M. Jafarian, M. Arjomandi, G.J. Nathan, A hybrid solar chemical looping combustion system with a high solar share, Appl. Energy 126 (2014) 69–77, https://doi.org/10.1016/j.apenergy.2014.03.071.

[49] M. Jafarian, M. Arjomandi, G.J. Nathan, The energetic performance of a novel hybrid solar thermal & chemical looping combustion plant, Appl. Energy 132 (2014) 74–85, https://doi.org/10.1016/j.apenergy.2014.06.052.

[50] M. Jafarian, M. Arjomandi, G.J. Nathan, Influence of the type of oxygen carriers on the performance of a hybrid solar chemical looping combustion system, Energy Fuel 28 (5) (2014) 2914–2924, https://doi.org/10.1021/ef402542b.

[51] Y. Liu, Q. Zhu, T. Zhang, X. Yan, R. Duan, Analysis of chemical-looping hydrogen production and power generation system driven by solar energy, Renew. Energy 154 (2020) 863–874, https://doi.org/10.1016/j.renene.2020.02.109.

[52] K. Svoboda, A. Siewiorek, D. Baxter, J. Rogut, M. Punčochář, Thermodynamic possibilities and constraints of pure hydrogen production by a chromium, nickel, and manganese-based chemical looping process at lower temperatures, Chem. Pap. 61 (2) (2007) 110–120, https://doi.org/10.2478/s11696-007-0007-6.

[53] S. Champagne, D.Y. Lu, A. MacChi, R.T. Symonds, E.J. Anthony, Influence of steam injection during calcination on the reactivity of CaO-based sorbent for carbon capture, Ind. Eng. Chem. Res. 52 (6) (2013) 2241–2246, https://doi.org/10.1021/ie3012787.

[54] Y.A. Criado, B. Arias, J.C. Abanades, Calcium looping CO_2 capture system for back-up power plants, Energy Environ. Sci. 10 (9) (2017) 1994–2004, https://doi.org/10.1039/c7ee01505d.

[55] K.N. Hutchings, M. Wilson, P.A. Larsen, R.A. Cutler, Kinetic and thermodynamic considerations for oxygen absorption/desorption using cobalt oxide, Solid State Ionics 177 (1–2) (2006) 45–51, https://doi.org/10.1016/j.ssi.2005.10.005.

[56] A. Steinfeld, P. Kuhn, J. Karni, High-temperature solar thermochemistry: production of iron and syntehsis gas by Fe_3O_4 reduction with methane, Energy 18 (3) (1993) 239–249.

[57] S. Hurst, Production of hydrogen by the steam-iron method, Oil Soap 16 (1939) 29–35.

[58] R.D. Woods, Rules of Thumb in Engineering Practice, Wiley-VCH, Weinheim, 2007.

[59] S. Dixon, C. Hall, Fluid Mechanics and Thermodynamics of Turbomachinery, Elsevier, 2014.

[60] A.P. Hinderink, F.P.J.M. Kerkhof, A.B.K. Lie, J. De Swans Aarons, H.J. Van der Kooi, Exergy analysis with a flowsheeting simulator - I. Theory; calculating exergies of material streams, Chem. Eng. Sci. 51 (20) (1996).

[61] J. Szargut, Chemical exergies of the elements, Appl. Energy 32 (1989) 269–286.

[62] G. Manzolini, E. MacChi, M. Gazzani, CO_2 capture in integrated gasification combined cycle with SEWGS - part B: economic assessment, Fuel 105 (2013) 220–227, https://doi.org/10.1016/j.fuel.2012.07.043.

[63] DOE/NETL, Cost and performance for low-rank pulverized coal oxycombustion energy plants, in: Tech. Rep., No. September, 2010, p. 442 [Online]. Available: https://www.globalccsinstitute.com/archive/hub/publications/119786/cost-performance-low-rank-pulverized-coal-oxycombustion-energy-plants.pdf.

[64] H. Thunman, C. Gustavsson, A. Larsson, I. Gunnarsson, F. Tengberg, Economic assessment of advanced biofuel production via gasification using cost data from the GoBiGas plant, Energy Sci. Eng. 7 (1) (2019) 217–229, https://doi.org/10.1002/ese3.271.

[65] E. De Lena, et al., Techno-economic analysis of calcium looping processes for low CO_2 emission cement plants, Int. J. Greenh. Gas Control 82 (October 2018) (2019) 244–260, https://doi.org/10.1016/j.ijggc.2019.01.005.

[66] S. Michalski, D.P. Hanak, V. Manovic, Techno-economic feasibility assessment of calcium looping combustion using commercial technology appraisal tools, J. Clean. Prod. 219 (2019) 540–551, https://doi.org/10.1016/j.jclepro.2019.02.049.

[67] A. Pizzolato, F. Donato, V. Verda, M. Santarelli, A. Sciacovelli, CSP plants with thermocline thermal energy storage and integrated steam generator – techno-economic modeling and design optimization, Energy 139 (2017) 231–246, https://doi.org/10.1016/j.energy.2017.07.160.

[68] S. Flegkas, F. Birkelbach, F. Winter, H. Groenewold, A. Werner, Profitability analysis and capital cost estimation of a thermochemical energy storage system utilizing fluidized bed reactors and the reaction system $MgO/Mg(OH)_2$, Energies 12 (24) (2019), https://doi.org/10.3390/en12244788.

[69] C. Ortiz, J.M. Valverde, R. Chacartegui, L.A. Perez-Maqueda, Carbonation of limestone derived CaO for thermochemical energy storage: from kinetics to process integration in concentrating solar plants, ACS Sustain. Chem. Eng. 6 (5) (2018) 6404–6417, https://doi.org/10.1021/acssuschemeng.8b00199.

[70] P. Charvin, S. Abanades, G. Flamant, F. Lemort, Two-step water splitting thermochemical cycle based on iron oxide redox pair for solar hydrogen production, Energy 32 (7) (2007) 1124–1133, https://doi.org/10.1016/j.energy.2006.07.023.

[71] U. Muschelknatuz, E. Muschelknatuz, Abscheideleistung von Rückführzyklonen in Wirbelschichtfeuerungen, VGB Kraftwerkstech. 79 (4) (1999) 58–63.

[72] S. Walas, Chemical Process Equipment, Elsevier, 1988, https://doi.org/10.1016/C2009-0-25916-2.

[73] U.S. Energy Information Administration. https://www.eia.gov/todayinenergy/detail.php?id=55119.

[74] G. Glenk, S. Reichelstein, Economics of converting renewable power to hydrogen, Nat. Energy 4 (March) (2019), https://doi.org/10.1038/s41560-019-0326-1.

[75] P. Psarras, S. Comello, P. Bains, P. Charoensawadpong, S. Reichelsten, J. Wilcox, Carbon capture and utilization in the industrial sector, Environ. Sci. Technol. 51 (2017) 11440–11449.

[76] M. Micari, K.V. Agrawal, Oxygen enrichment of air: performance guidelines for membranes based on techno-economic assessment, J. Membr. Sci. 641 (July 2021) (2022) 119883, https://doi.org/10.1016/j.memsci.2021.119883.

[77] B. Adhikari, C.J. Orme, J.R. Klaehn, F.F. Stewart, Technoeconomic analysis of oxygen-nitrogen separation for oxygen enrichment using membranes, Sep. Purif. Technol. 268 (February) (2021) 118703, https://doi.org/10.1016/j.seppur.2021.118703.

[78] European Commission, Guide to Cost-benefit Analysis of Investment Projects: Economic Appraisal Tool for Cohesion Policy 2014–2020, No. December, 2014, https://doi.org/10.2776/97516.

[79] D.P. Hanak, V. Manovic, Economic feasibility of calcium looping under uncertainty, Appl. Energy 208 (June) (2017) 691–702, https://doi.org/10.1016/j.apenergy.2017.09.078.

[80] US, US Geological Survey. https://www.usgs.gov/centers/nmic/iron-and-steel-statistics-and-information?qt-science_support_page_related_con=0, 2022.

[81] INTRATEC, Cooling water current costs, historical series and forecasts. https://www.intratec.us/products/water-utility-costs/commodity/cooling-water-cost#.

[82] M. Younas, S. Shafique, A. Hafeez, F. Javed, F. Rehman, An overview of hydrogen production: current status, potential, and challenges, Fuel 316 (February) (2022) 123317, https://doi.org/10.1016/j.fuel.2022.123317.

[83] A. Muto, T. Hansen, Demonstration of high-temperature calcium-based thermochemical energy storage system for use with concentrating solar power facilities [Online]. Available: https://www.osti.gov/servlets/purl/1523643, 2018.

[84] R. Porrazzo, G. White, R. Ocone, Techno-economic investigation of a chemical looping combustion based power plant, Faraday Discuss. 192 (2016) 437–457, https://doi.org/10.1039/c6fd00033a.

[85] P. Breeze, The Cost of Electricity, Elsevier, 2021, https://doi.org/10.1016/C2020-0-01014-5.

[86] C.K. Ho, A review of high-temperature particle receivers for concentrating solar power, Appl. Therm. Eng. 109 (2016) 958–969, https://doi.org/10.1016/j.applthermaleng.2016.04.103.

[87] J. Santos, J. Palacio, A. Reyes, M. Carvalho, A. Freire, M. Barone, Concentrating solar power: clean power on demand 24/7, Conc. Sol. Power Clean Power Demand 24 (7) (2018) 373–402 [Online]. Available: www.worldbank.org.

[88] The World Bank, Carbon pricing dashboard. https://carbonpricingdashboard.worldbank.org/map_data, 2023.

[89] S. Alavand, J. Seaba, G. Subbaraman, Emerging and existing oxygen production technology scan and evaluation, Des Plaines, Illinois, 2018 [Online]. Available: www.gastechnology.org.

[90] IEA, Global Hydrogen Review, 2022.

[91] IEA, Outlook for biogas and biomethane: prospects for organic growth [Online]. Available: https://www.iea.org/reports/outlook-for-biogas-and-biomethane-prospects-for-organic-growth, 2020.